

On the precision of full-spectrum fitting of simple stellar populations. II. The dependence on star cluster mass in the wavelength range 0.3 – 5.0 μm .

Paul Goudfrooij¹★ and Randa S. Asa’d^{2,1}

¹*Space Telescope Science Institute, 3700 San Martin Drive, Baltimore, MD 21218, USA*

²*Physics Department, American University of Sharjah, P.O. Box 26666, Sharjah, UAE*

Accepted XXX. Received XXX; in original form 2020 XXX

ABSTRACT

In this second paper of a series on the accuracy and precision of the determination of age and metallicity of simple stellar populations (SSPs) by means of the full spectrum fitting technique, we study the influence of star cluster mass through stochastic fluctuations of the number of stars near the top of the stellar mass function, which dominate the flux in certain wavelength regimes depending on the age. We consider SSP models based on the Padova isochrones, spanning the age range $7.0 \leq \log(\text{age/yr}) \leq 10.1$. Simulated spectra of star clusters in the mass range $10^4 \leq M/M_\odot < 10^6$ are compared with SSP model spectra to determine best-fit ages and metallicities using a full-spectrum fitting routine in four wavelength regimes: the blue optical (0.35–0.70 μm), the red optical (0.6–1.0 μm), the near-IR (1.0–2.5 μm), and the mid-IR (2.5–5.0 μm). We compare the power of each wavelength regime in terms of both the overall precision of age and metallicity determination, and of its dependence on cluster mass. We also study the relevance of spectral resolution in this context by utilizing two different spectral libraries (BaSeL and BT-Settl). We highlight the power of the mid-IR regime in terms of identifying young massive clusters in dusty star forming regions in distant galaxies. The spectra of the simulated star clusters and SSPs are made available online to enable follow-up studies by the community.

Key words: stars: abundances – stars: luminosity function, mass function – star clusters: general

1 INTRODUCTION

Star clusters are generally considered to be the best known examples of simple stellar populations (SSPs). They constitute compact stellar systems containing thousands to millions of stars with essentially the same age and metallicity. Star clusters are also highly relevant for galaxy formation and evolution studies, since a significant fraction of star formation occurs in clusters (e.g., Lada & Lada 2003). Since clusters can be observed with useful signal-to-noise ratios out to distances of tens to hundreds of Mpc, they are key to providing important clues of the star formation and chemical enrichment history of their host galaxies by means of measurements of their ages, metallicities, and masses (e.g., Brodie & Strader 2006; Goudfrooij et al. 2007; Goudfrooij 2012; Fall et al. 2009; Chandar et al. 2010; Chilingarian & Asa’d 2018). Observational studies of cluster populations in galaxies depend critically on two basic limitations and how to deal with them: (1) observational biases in terms of photometric and spatial completeness fractions of various cluster samples. For example, young cluster populations tend to be found in star formation regions with strong and spatially variable amounts of extinction, which causes a wavelength dependence to completeness fractions which impact the low-luminosity end of cluster luminosity functions; (2) the limited accuracy and precision of methods to estimate cluster ages, metallicities, and masses.

With the exception of star clusters in galaxies within the Local

Group, one has to use integrated-light measurements to estimate their properties. This estimation involves the use of synthetic stellar population synthesis (SPS) models, which generally assume that the initial mass function (IMF) of stellar systems is uniformly populated, i.e., that the distribution of stellar masses is continuous and that all the evolutionary stages are well sampled. However, this assumption is incorrect for real star clusters due to their finite mass. Hence, the level of validity of a comparison between the predictions of synthesis models and observations of real clusters depends on the cluster mass. This phenomenon is often referred to as “stochastic fluctuations” and is due to the confluence of the small fractional number of bright stars in a stellar population and their large contribution to the luminosity. Random sampling of the stellar mass function can thus cause significant changes in the resulting spectral energy distribution (SED) of star clusters (e.g., Girardi & Bica 1993; Santos & Frogel 1997; Lançon & Mouhcine 2000), leading to incorrect determinations of cluster ages and masses.

The effects of stochastic fluctuations on photometric observations of star clusters have been studied by several teams (e.g., Lançon & Mouhcine 2000; Cerviño & Luridiana 2004, 2006; Piskunov et al. 2009; Popescu & Hanson 2009; Popescu et al. 2012; Fouesneau & Lançon 2010; Fouesneau et al. 2012, 2014; Krumholz et al. 2015, 2019). These studies have shown that the predicted colour distributions depend strongly on the cluster mass (especially in the near-IR regime) and that they can be significantly non-Gaussian, even for cluster masses exceeding $10^5 M_\odot$. Best-fit ages derived by comparing the colours of low-mass mock clusters with standard SPS model

★ e-mail: goudfroo@stsci.edu

predictions have been found to concentrate around certain discrete ages corresponding to significant and luminous events in stellar evolution such as the sudden onset of supergiants, the upper asymptotic giant branch (AGB), and the red giant branch (RGB). This standard method often underestimates cluster ages significantly by up to 1.5 dex, a precision that can be improved significantly by using mass-dependent colours produced using “discrete” population synthesis (Popescu & Hanson 2010a,b; Fouesneau & Lançon 2010; Krumholz et al. 2019).

In the current paper, we expand the investigation of the effects of stochastic fluctuations as a function of wavelength to analyze results obtained from the full-spectrum fitting method, which has become popular through its virtue of incorporating all features in the SED of stellar systems. While this method is more sensitive to the accuracy of flux calibration than the other popular method of index fitting using equivalent widths of spectral features (e.g., Worthey 1994; Schiavon 2007), it uses the continuum shape as well as all spectral lines, which can significantly improve the precision of age determination (Bica & Alloin 1986; Santos et al. 1995; Santos et al. 2006; Cid Fernandes & Gonzalez Delgado 2010; Sánchez-Blázquez et al. 2011; Benítez-Llambay et al. 2012; Asa'd 2014; Wilkinson et al. 2017; Chilingarian & Asa'd 2018).

In Asa'd & Goudfrooij (2020, hereafter paper I), we investigated the precision of age and metallicity estimation using the method of full-spectrum fitting of integrated-light spectra as functions of the S/N of the data and the wavelength range used in the fitting within the optical wavelength regime. In this second paper of the series, we examine the dependence of the precision of this fitting technique on the mass of the star cluster, through its effects of random sampling of the stellar mass function. We perform this analysis for the age range $7.0 \leq \log(\text{age/yr}) \leq 10.1$ in four different wavelength ranges from the optical through mid-IR regimes ($0.3\text{--}5.0\ \mu\text{m}$), thus providing relevant information on the power of those wavelength regimes in terms of the precision of the determination of ages, metallicities, and masses of star clusters. These results are relevant for both optical and near-IR (NIR) spectroscopy as well as future space-based spectroscopy such as with the NIR instruments aboard the James Webb Space Telescope (JWST).

The simulations and methods are described in Section 2, followed by a detailed discussion of the results in Section 3. We summarize our findings in Section 4.

2 DATA AND METHODS

2.1 Mock Star Clusters and their Integrated-light Spectra

2.1.1 Methodology

For the purposes of this paper, all stars in a star cluster are presumed to have the same age and chemical abundance. This constitutes a simplification of the real situation, since most old globular clusters are now known to host variations of abundances of several light elements (mainly He, C, N, O, Na, and Al; see Bastian & Lardo 2018 and references therein). However, these variations seem to be absent in clusters younger than ~ 2 Gyr (see Martocchia et al. 2018), and the purpose of this paper is to test the influence of cluster mass on the precision of the determination of ages and metallicities of integrated-light spectra. As such, we treat star clusters as SSPs, we assume solar element abundance ratios, and we ignore the influence of binary stars.

Star clusters with masses between $10^4 M_\odot$ and $10^6 M_\odot$ are simulated as described in detail in Goudfrooij et al. (2009, 2011). Briefly,

we populate Padova isochrones from Marigo et al. (2008) with stars randomly drawn from a Kroupa (2001) initial mass function (IMF) between the minimum ($0.15 M_\odot$) and the maximum stellar mass in the isochrone table in question. The total number of stars N in a cluster simulation is determined as follows:

$$N = M_{\text{cl}} / \overline{M}_* \quad (1)$$

where M_{cl} is the cluster mass and \overline{M}_* is the mean stellar mass in the isochrone for the Kroupa (2001) IMF (see also Popescu & Hanson 2009). For each star in the simulation, values for $\log L$, $\log T_{\text{eff}}$, and $\log g$ are determined by means of linear interpolation between entries in the relevant isochrone, using the initial stellar mass $M_{*,i}$ as the independent variable. The number of independent cluster simulations for a given cluster mass was chosen to produce a grand total of $5 \times 10^6 M_\odot$ at each age. We created these simulated clusters for a grid in $\log(\text{age/yr})$ between 7.0 and 10.1 with a step size $\Delta \log(\text{age/yr}) = 0.1$. As in paper I, we adopt a fixed cluster metallicity of $[Z/H] = -0.4$ for this study (corresponding to the metallicity of the Large Magellanic Cloud (LMC)).

Integrated-light spectra are derived for each simulated cluster by creating and co-adding spectra of all constituent stars, using a script INTSPEC which involves M. Fouesneau’s `pystellib`¹ tools in Python, featuring 2-D linear interpolation in $\log T_{\text{eff}} - \log g$ space and linear interpolation in metallicity. To enable a comparison between spectral libraries in terms of model ingredients as well as spectral resolution, we use two synthetic libraries:

(i) BaSeL (Lejeune et al. 1998) which comprises a theoretical Kurucz library that was recalibrated using empirical photometry. This recalibration is defined for the metallicity range $-1.0 < [Z/H] < +0.5$ for both dwarf and giant stars. The spectral resolution of the BaSeL library is $20\ \text{\AA}$ in the wavelength range $2900\ \text{\AA} - 1\ \mu\text{m}$, $50\ \text{\AA}$ ($1.0 - 1.6\ \mu\text{m}$), $100\ \text{\AA}$ ($1.6 - 3.2\ \mu\text{m}$), $200\ \text{\AA}$ ($3.2 - 6.4\ \mu\text{m}$), and $400\ \text{\AA}$ ($6.4 - 10.0\ \mu\text{m}$).

(ii) BT-Settl (Allard et al. 2012) which is based on the Phoenix code with updates for water vapor, methane, ammonia and CO_2 , as well as a cloud model that uses 2-D radiation hydrodynamic simulations. The spectral resolution of the BT-Settl library is $2\ \text{\AA}$ ($\lambda \leq 1.05\ \mu\text{m}$), $4\ \text{\AA}$ ($1.05 - 2.5\ \mu\text{m}$), $16\ \text{\AA}$ ($2.5 - 5.4\ \mu\text{m}$), $160\ \text{\AA}$ ($5.4 - 30\ \mu\text{m}$), and $0.8\ \mu\text{m}$ ($30 - 80\ \mu\text{m}$).

The main reasons why we use synthetic libraries in this paper are their spectral coverage across the full wavelength range considered here (which is particularly relevant to space-based observations) and their uniform coverage in $\log T_{\text{eff}} - \log g - [Z/H]$ parameter space. In this paper, we only consider wavelengths up to $5\ \mu\text{m}$, since the BaSeL library uses blackbody spectra beyond that.

2.1.2 Caveats

It should be noted that the BaSeL and BT-Settl libraries do not include spectra of carbon stars, which are important in stellar population synthesis of intermediate-age populations when the contribution of cool, thermally pulsing AGB stars to integrated-light spectra is significant (e.g., Lançon & Mouhcine 2002; Maraston 2005; Conroy et al. 2009). For example, the number ratio of carbon stars to M-type (i.e., oxygen-rich) AGB stars can be used as an indirect indication of the metallicity at the formation era (e.g., Cioni & Habing 2005). The omission of carbon stars in stellar libraries will therefore have a negative effect on the *absolute* accuracy and precision of metallicity determination in

¹ <http://mfouesneau.github.io/docs/pystellib>

intermediate-age populations. However, the actual relation between the C/O number ratio of AGB stars and the metallicity is still quite uncertain (e.g., [Boyer et al. 2019](#)). Moreover, the focus of this paper is on the effect of *cluster mass*, and the associated stochastic fluctuations of the distribution of stars across the luminous post-MS stages of stellar evolution in isochrones, on the resulting precision of age and metallicity determination for star cluster spectra. With this in mind, we use the BaSeL and BT-Settl libraries as is, thus modeling AGB stars as oxygen-rich M-type stars.

Our SED modeling also does not include the effects of circumstellar dust around cool AGB stars (with $T_{\text{eff}} \lesssim 4000$ K). As shown by [Villaume et al. \(2015\)](#), the emission from such dust has an appreciable contribution to the SED for $\lambda \gtrsim 4\mu\text{m}$ for SSPs with ages in the range 0.2–5 Gyr. Its contribution generally increases with λ (up to $\sim 20\mu\text{m}$), and decreases with increasing metallicity. However, the effect stays very moderate at $\lambda \leq 5\mu\text{m}$ at the metallicity of the LMC. We will discuss the possible impact of circumstellar dust emission to our results in Section 3.4.

Finally, we also do not include blue horizontal branch (BHB) stars in our SED modeling. The high T_{eff} of such HB stars in globular clusters (up to $\approx 30,000$ K) has received extensive attention in the literature, and is generally thought to be due to two possible causes that aren’t well understood, and not modeled in standard isochrones: a metallicity-dependent mass loss rate on the RGB (e.g., [Greggio & Renzini 1990](#)) and/or a cluster mass-dependent fraction of stars with high helium abundance (e.g., [Brown et al. 2016](#); [Goudfrooij 2018](#); [Milone et al. 2018](#)). In the context of this paper, the main relevance of hot BHB stars is that their presence increases the equivalent widths of hydrogen absorption lines, and thus makes spectra of old clusters look younger than they really are ([Lee et al. 2000](#); [Maraston & Thomas 2000](#)). However, with adequate signal-to-noise ratio and spectral resolution, the spectral signatures of a BHB can actually be recognized in optical spectra (e.g., [Schiavon et al. 2004](#); [Trager et al. 2005](#)). Furthermore, direct evidence of such “apparent youth” due to BHB stars among globular clusters with metallicities in the range considered here (i.e., $[Z/H] > -1$) has so far only been found in NGC 6388 and NGC 6441 (e.g., [Maraston et al. 2003](#)), two of the most massive globular clusters in our Galaxy ($\log(M/M_\odot) \sim 6.5$), while metal-rich globular clusters with masses $\lesssim 10^6 M_\odot$ do not show evidence for BHB stars (see [Milone et al. 2018](#)). It therefore seems unlikely that the omission of this effect has a significant impact on our results, given the cluster masses considered in this paper.

2.2 SSP fitting method

To compare the synthetic integrated-light spectra of the simulated clusters with SSP model predictions, we create sets of integrated-light spectra of “idealized” SSPs (i.e., clusters of “pseudo-infinite” mass) using a script `SSPSPEC` which is similar to `INTSPEC` described above, except that the stars’ properties are taken directly from the isochrone entries. Each spectrum derived for the isochrone entries is then assigned a weight W_i that is proportional to the number of stars at that initial stellar mass, i.e., to the chosen IMF. Since isochrone models generally do not sample their entries with an uniform bin size in initial stellar mass (dM), we involve the latter in W_i as follows:

$$W_i = \frac{N_i(M - dM/2, M + dM/2)}{N_{\text{total}}} = \frac{\int_{M-dM/2}^{M+dM/2} \psi_i(M) dM}{\int_{m_{\text{min}}}^{m_{\text{max}}} \psi_i(M) M dM} \quad (2)$$

where N_{total} is the total number of stars in the SSP, $\psi(M) = dN/dM$ is the IMF, and m_{min} and m_{max} are the minimum and maximum initial stellar mass in the isochrone, respectively. The integrations are

performed numerically using adaptive quadrature. For the purpose of this paper, we use the same IMF, isochrone family, and spectral library as the mock cluster spectra. We create these SSP model spectra for the age range $6.8 < \log(\text{age/yr}) < 10.2$, again with a grid step size of 0.1 dex. This grid of SSP spectra is created for metallicities $[Z/H] = -1.0, -0.8, -0.6, -0.4, -0.2, 0.0$, and $+0.2$, thus staying within the range in which the BaSeL library was recalibrated using empirical photometry. All model spectra of mock clusters and SSPs created for this paper are made available in the online supplementary material of this article for follow-up studies by the community.

After converting both the mock cluster spectra and the SSP model spectra to a common flux normalization, we use the full-spectrum fitting routine `ASAD2` described in [Asa’d \(2014\)](#) and [Asa’d et al. \(2013, 2016\)](#) to obtain the best age and metallicity estimation by minimizing the following quantity:

$$\sum_{\lambda=\lambda_{\text{start}}}^{\lambda_{\text{end}}} \frac{[(CF)_\lambda - (MF)_\lambda]^2}{(CF)_{\lambda_{\text{norm}}}}, \quad (3)$$

where CF is the mock cluster spectrum, MF is the SSP model spectrum, and λ_{norm} is the wavelength where CF and MF are normalized to unity.

3 RESULTS AND DISCUSSION

Figures 1–3 illustrate the extent of variation in the 0.3–5 μm SED of SSPs introduced by the stochastic effects of a limited cluster mass for various ages and cluster masses between 10^4 and $10^6 M_\odot$. For the case of $10^4 M_\odot$ clusters, we show the level of variation both in units of $\log(F_\lambda)$ and $\log(F_\lambda/\bar{F}_\lambda)$, where \bar{F}_λ is the mean F_λ of all simulated clusters of a given cluster mass. (For the higher cluster masses, only $\log(F_\lambda/\bar{F}_\lambda)$ is shown.) A glance at these Figures immediately highlights a number of general properties of the effects of stochastic fluctuations as a function of wavelength: (1) the SED variations generally start to increase significantly beyond $\lambda \sim 7000$ Å; (2) the distribution of the variations generally is asymmetric and non-Gaussian, and the level of its asymmetry varies significantly with SSP age; and (3) the amplitude of the variations decreases strongly at strong molecular spectral features at ages in the approximate range $8.5 \lesssim \log(\text{age/yr}) \lesssim 9.0$. To help understand these properties, we plot all 500 individual simulated spectra for clusters with $M/M_\odot = 10^4$ for several ages in Figure 4.

For the remainder of this section, we split the discussion into four wavelength regimes: the blue optical (3500–7000 Å), the red optical (0.6–1.0 μm), the NIR (1.0–2.5 μm), and the mid-IR (2.5–5.0 μm). This choice is based on the results seen in Figures 1–4 as well as to highlight the differences in the power of full-spectrum fitting in terms of age and metallicity determination in those different wavelength regimes. To set the context for this discussion, we plot colour-magnitude diagrams (CMDs) involving filter passbands in these four wavelength regimes in Figures 5–8. Each of these Figures shows a grid of CMDs covering the full age range considered in this paper, thus depicting the relative luminosities of the various stages of stellar evolution as a function of age. For a subset of ages, Figures 5–8 also list the luminosity fractions produced by main sequence turnoff (MSTO) stars and post-MS stars for a Kroupa IMF, denoted by f_{MSTO} and $f_{\text{post-MS}}$, respectively. In the calculation of f_{MSTO} , we include stars from the tip of the MSTO down to 1 mag below the turnoff point on the CMD in this context. These luminosity fractions are relevant in the discussion of the impact of stochastic fluctuations for different ages and wavelength regimes.

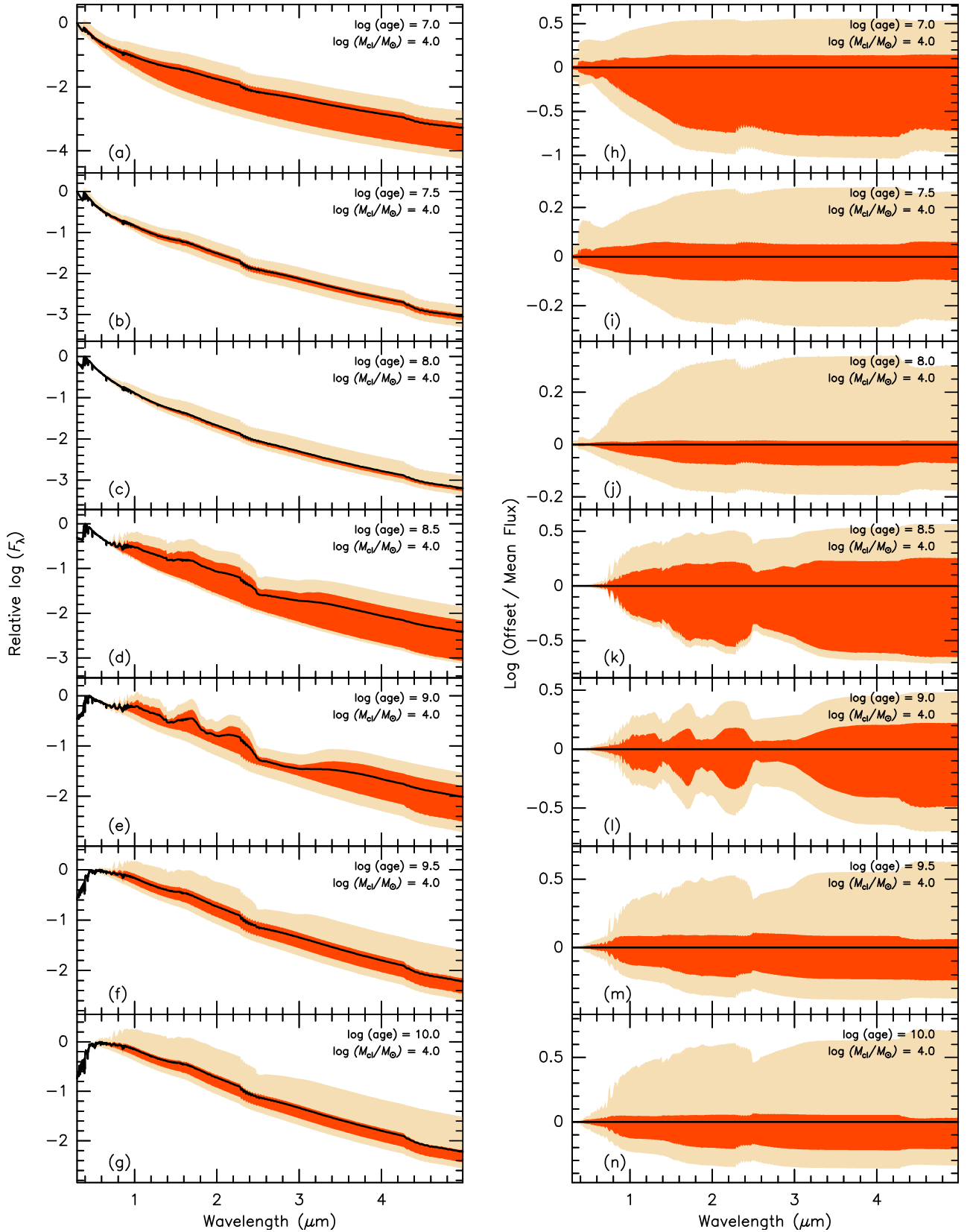


Figure 1. Star cluster SEDs and the effects of stochastic fluctuations of the number of stars near the top of the stellar mass function for a simulated cluster mass of $10^4 M_{\odot}$. The metallicity is $[Z/H] = -0.4$. *Left panels (a–g):* Cluster SEDs in $\log(F_{\lambda})$ vs. λ for $\log(\text{age/yr}) = 7.0, 7.5, 8.0, 8.5, 9.0, 9.5$, and 10.0 (see legend), using the BaSeL spectral library. The solid black line represents the mean SED of all simulated clusters at that age, normalized by its maximum F_{λ} . The beige shading indicates the full region occupied by the simulated cluster SEDs (using the same normalization), while the red shading indicates the region occupied by simulated cluster SEDs between 25% and 75% of the full distribution. *Right panels (h–n):* Same as left panels, but now plotted as the logarithm of the offset from the mean F_{λ} relative to the mean F_{λ} . Note the significant scatter at $\lambda \gtrsim 0.7 \mu\text{m}$, which is discussed in Section 3.

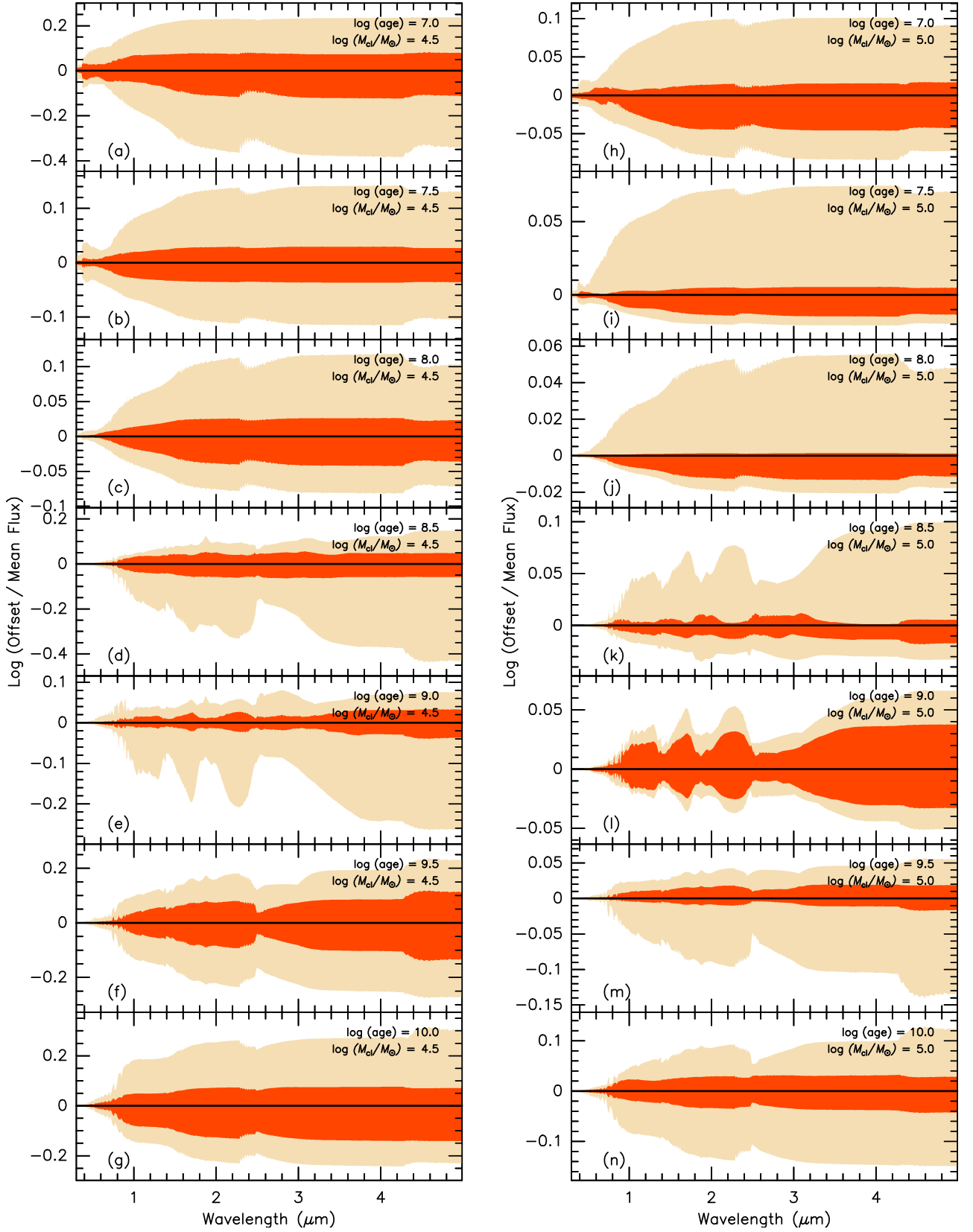


Figure 2. Left panels (a–g): Same as right panels in Figure 1, but now for a cluster mass of $3 \times 10^4 M_{\odot}$. Right panels (h–n): Same as left panels, but now for a cluster mass of $10^5 M_{\odot}$.

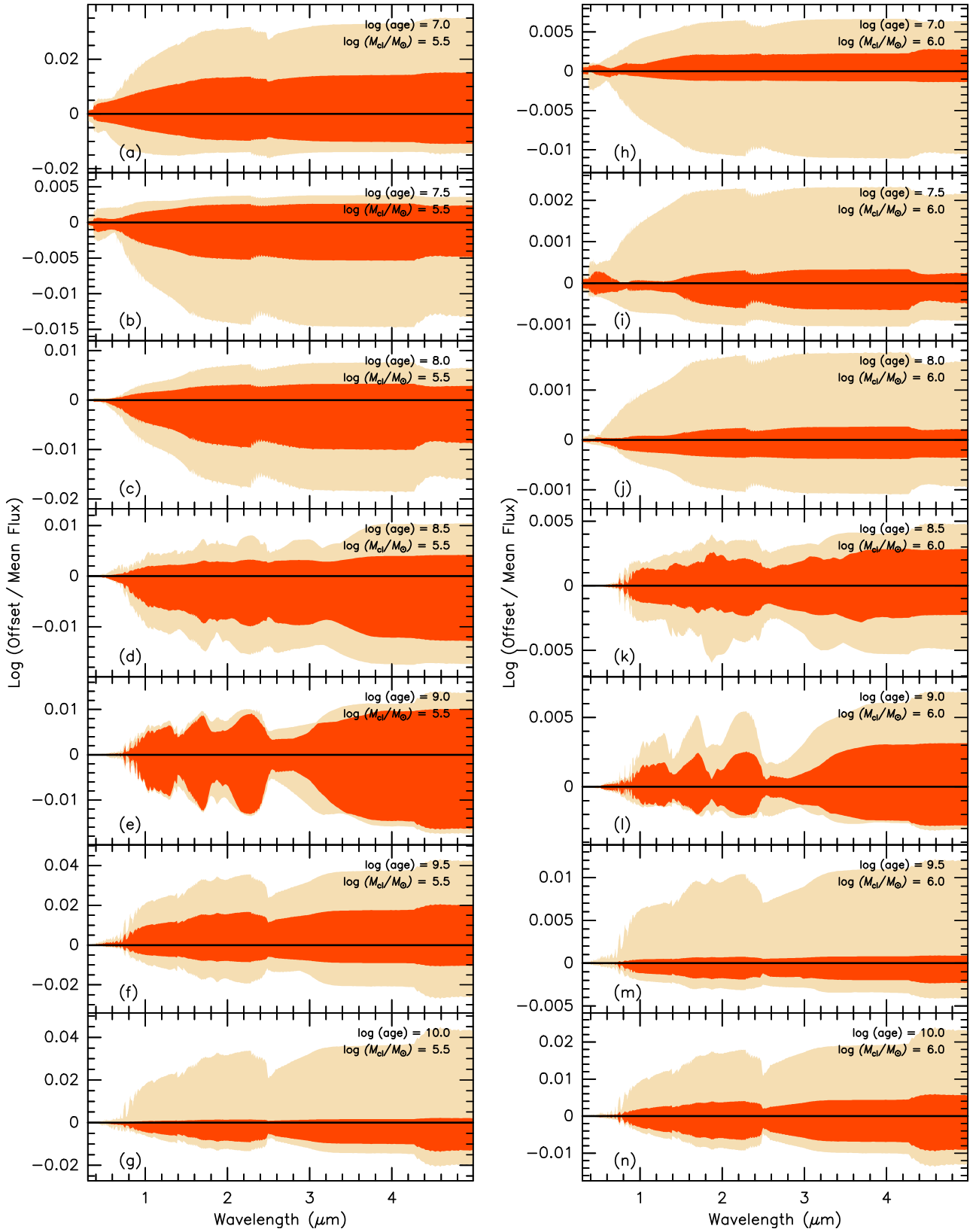


Figure 3. Left panels (a–g): Same as right panels in Figure 1, but now for a cluster mass of $3 \times 10^5 M_{\odot}$. Right panels (h–n): Same as left panels, but now for a cluster mass of $10^6 M_{\odot}$.

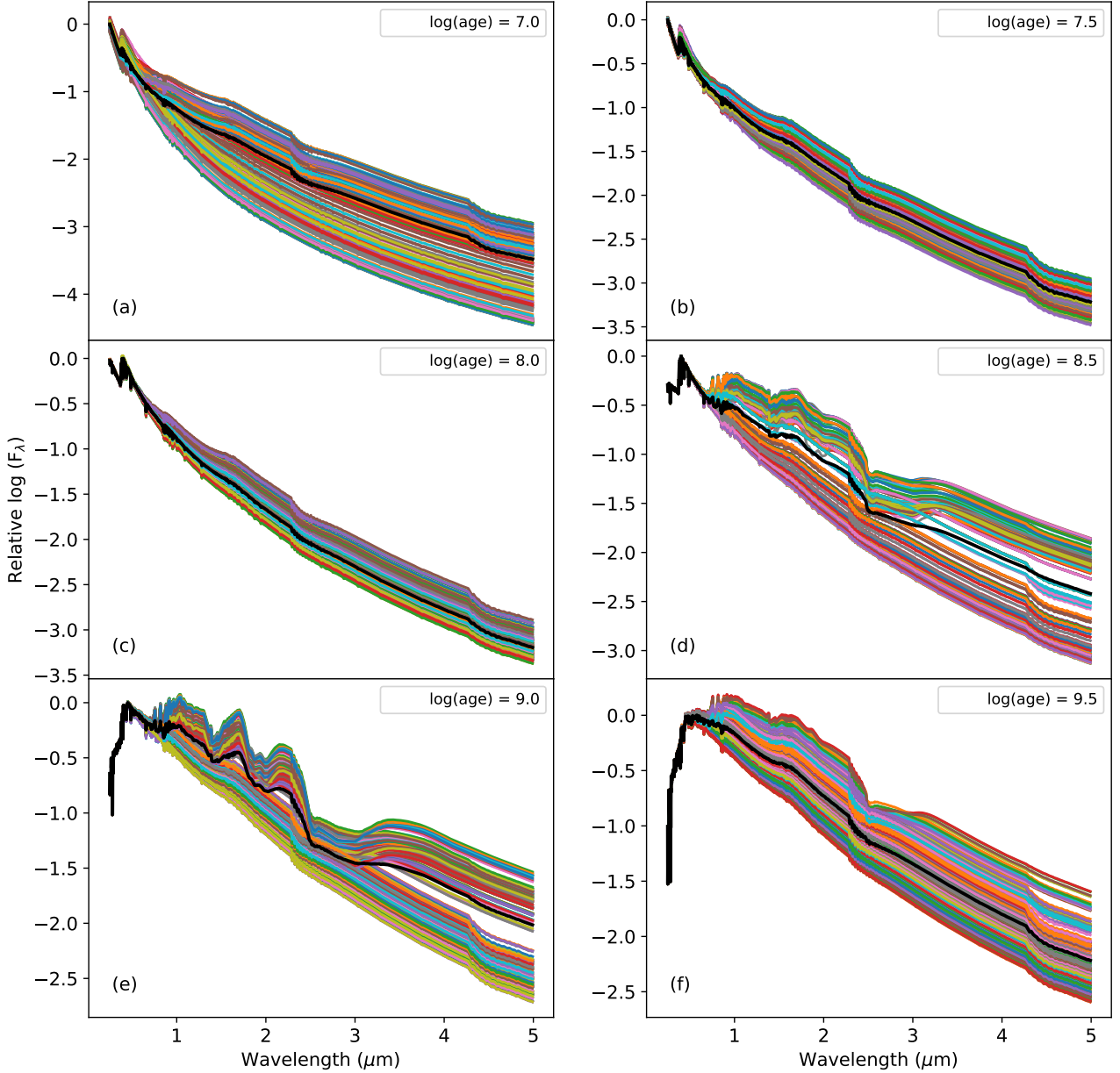


Figure 4. Similar to Figure 1, except that we now plot all 500 individual simulated $10^4 M_{\odot}$ cluster spectra for the $\log(\text{age}/\text{yr})$ values shown in the legends. The thick black line in each panel again represents the mean SED of all simulated clusters at that age, normalized by its maximum F_{λ} . All individual cluster spectra were divided by that normalization factor. See discussion in Section 3.

3.1 Blue Optical Range: 3500 – 7000 Å

The shape of cluster SEDs in this wavelength range is relatively insensitive to the stochastic fluctuations of the sampling of high-mass stars in the stellar MF, when compared with the situation at longer wavelengths. The main reason for this can be seen in B vs. $B - R$ CMDs of Padova isochrones, shown in Figure 5. Note that the MSTO region, which is much more densely populated with stars than the post-MS stages of stellar evolution, accounts for a high luminosity fraction in this wavelength range for almost all ages relative to the situation at longer wavelengths (cf. Figures 6, 7, and 8). And indeed, as shown in the right-hand panels of Figure 1 for the simulated clusters with the lowest considered mass of $10^4 M_{\odot}$, we find that even for the ages that show the strongest variation of SED shape (i.e.,

$\log(\text{age}) \leq 7.5$), the FWHM values of the distributions of differences relative to the true SSP SED stay within 10%, gradually decreasing with increasing cluster mass and dropping below 1% at $M \sim 10^5 M_{\odot}$.

We now address how this translates into the precision of age and metallicity determination using full-spectrum fitting in the blue optical range as a function of cluster mass. We normalize the spectra in this wavelength range following Paper 1, using $\lambda_{\text{norm}} = 5870 \text{ Å}$ (cf. Equation 3) during the fitting procedure. For the purpose of quantifying fitting results, we define the “success rate” as the fraction of clusters whose age or metallicity are recovered correctly to within 0.1 dex. Figure 9 depicts this “success rate” as functions of age and cluster mass, while Figures A1 and A2 (in the Appendix) shows the actual distributions of relative fractions of offsets from true $\log(\text{age})$ and $[Z/H]$ seen among all the simulated clusters. For the lowest-mass

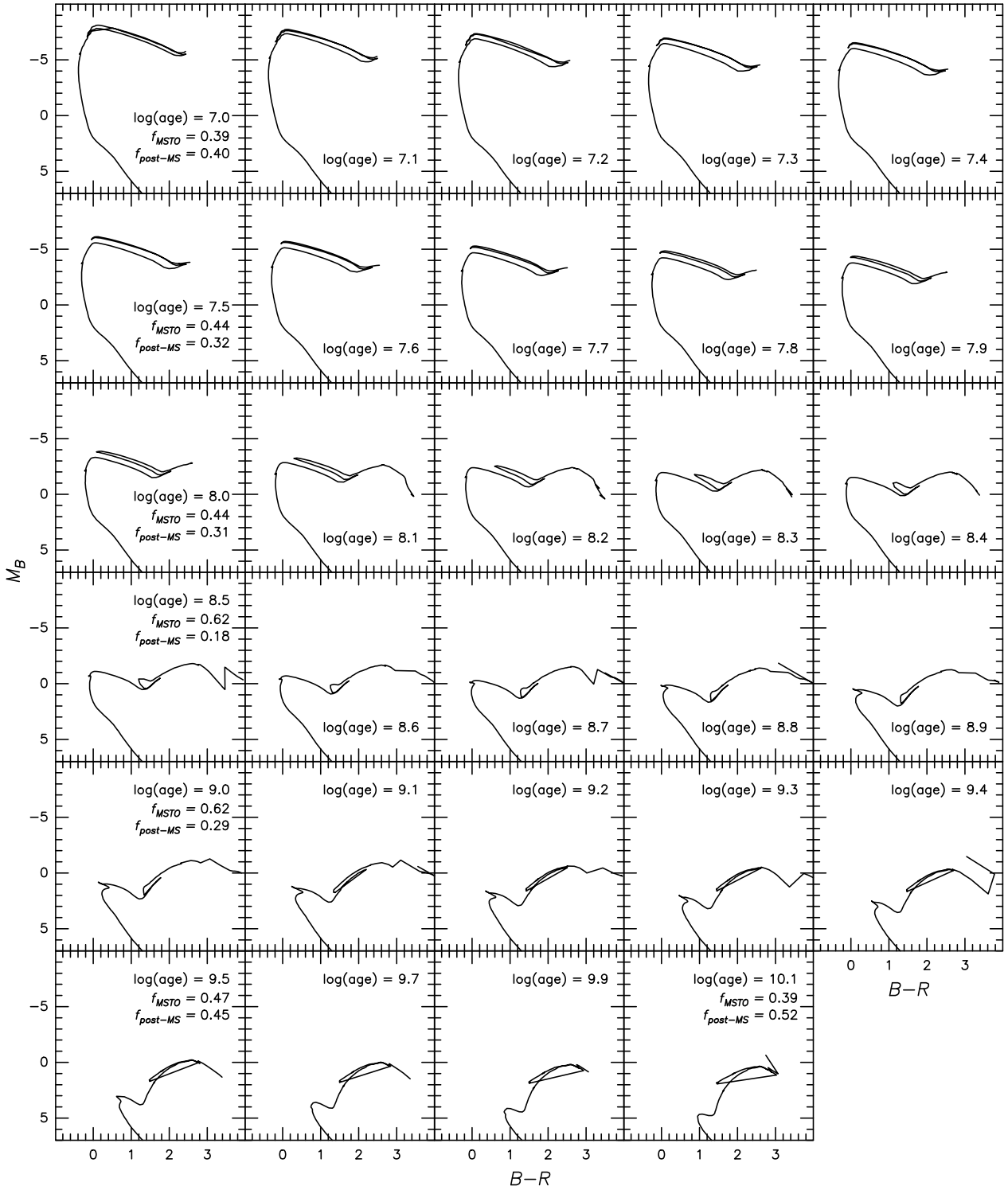


Figure 5. Blue optical range: B vs. $B - R$ CMDs for Padova isochrones with $[Z/H] = -0.4$ and $7.0 \leq \log(\text{age/yr}) \leq 10.1$ (see legend in each panel). For $\log(\text{age/yr}) = 7.0, 7.5, 8.0, 8.5, 9.0, 9.5$, and 10.1 , the legend also shows the values of f_{MSTO} and $f_{\text{post-MS}}$, which are the B -band luminosity fractions of MSTO stars and the post-MS stars, respectively, for a Kroupa IMF. See Section 3.1 for details.

clusters considered here (i.e., $10^4 M_{\odot}$), the success rate ranges between roughly 40% and 100% for $\log(\text{age})$, depending on the age. Metallicity determination does not fare as well, ranging between success rates of just a few % at the youngest ages and $\sim 75\%$ at ages of $\gtrsim 1.5$ Gyr. This generally poorer recovery of metallicity relative

to that of age is partly intrinsic to the method of full-spectrum fitting, since the wavelength coverage of spectra by stellar continuum is generally larger than that by strong spectral lines, and continuum shape is more sensitive to age than to metallicity (see, e.g., [Bica & Alloin 1986](#); [Benítez-Llambay et al. 2012](#)). The precision of both age

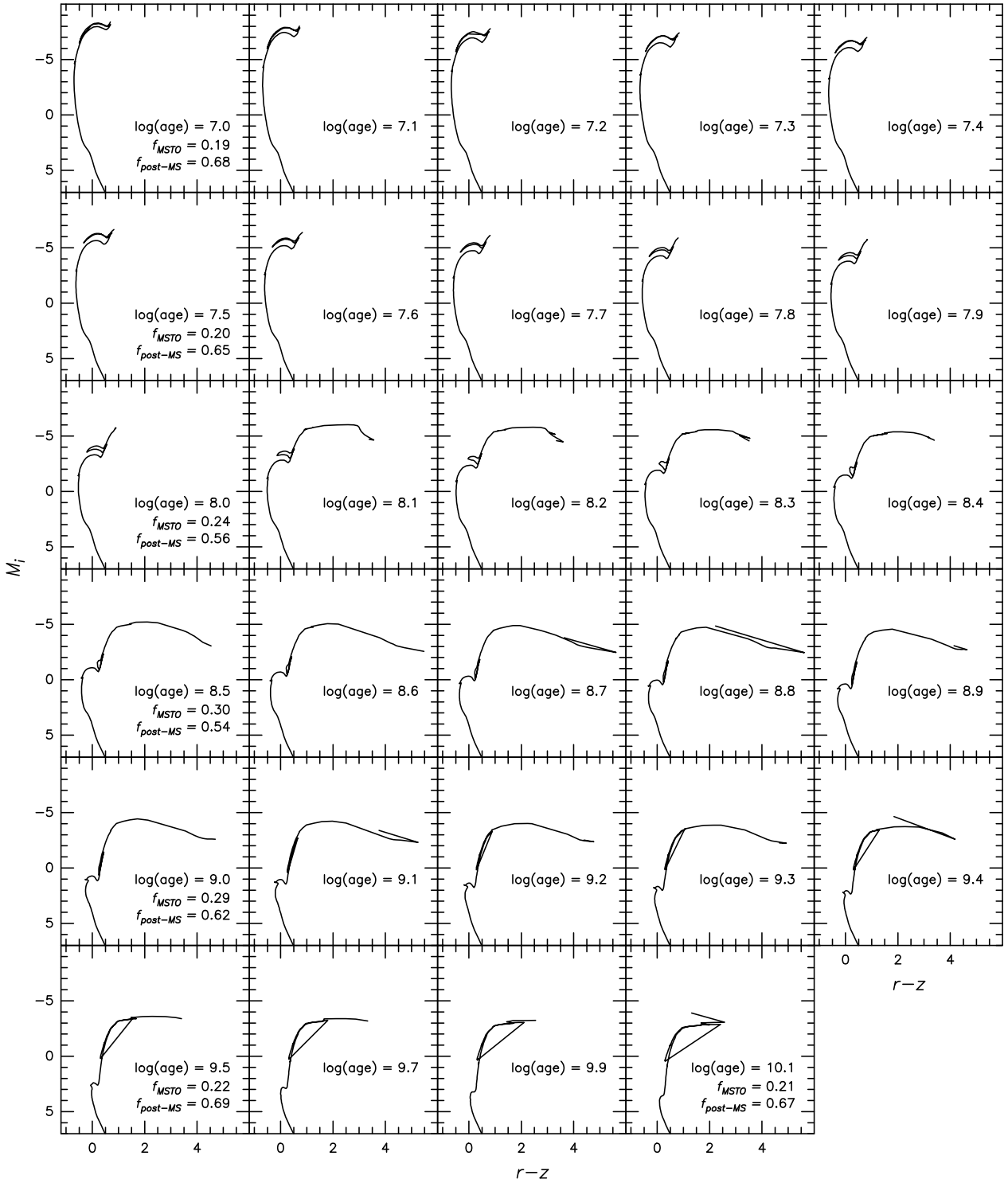


Figure 6. Similar to Figure 5 but now for the red optical range: i_{SDSS} vs. $(r-z)_{\text{SDSS}}$ CMDs for Padova isochrones with $[Z/H] = -0.4$ and $7.0 \leq \log(\text{age/yr}) \leq 10.1$ (see legend in each panel). Values for f_{MSTO} and $f_{\text{post-MS}}$ now refer to i_{SDSS} -band luminosities

and metallicity determination generally improves significantly with increasing cluster mass, with the exception of metallicity at ages $\lesssim 300$ Myr. The latter is likely due to the absence of strong metallic lines in the blue optical regime for hot stars (see Figure 10). Finally, a comparison of the success rates derived for the BaSeL and BT-Settl

libraries (see panels (a)–(d) vs. panels (e)–(h) of Figure 9) reveals no significant differences for the blue optical regime.

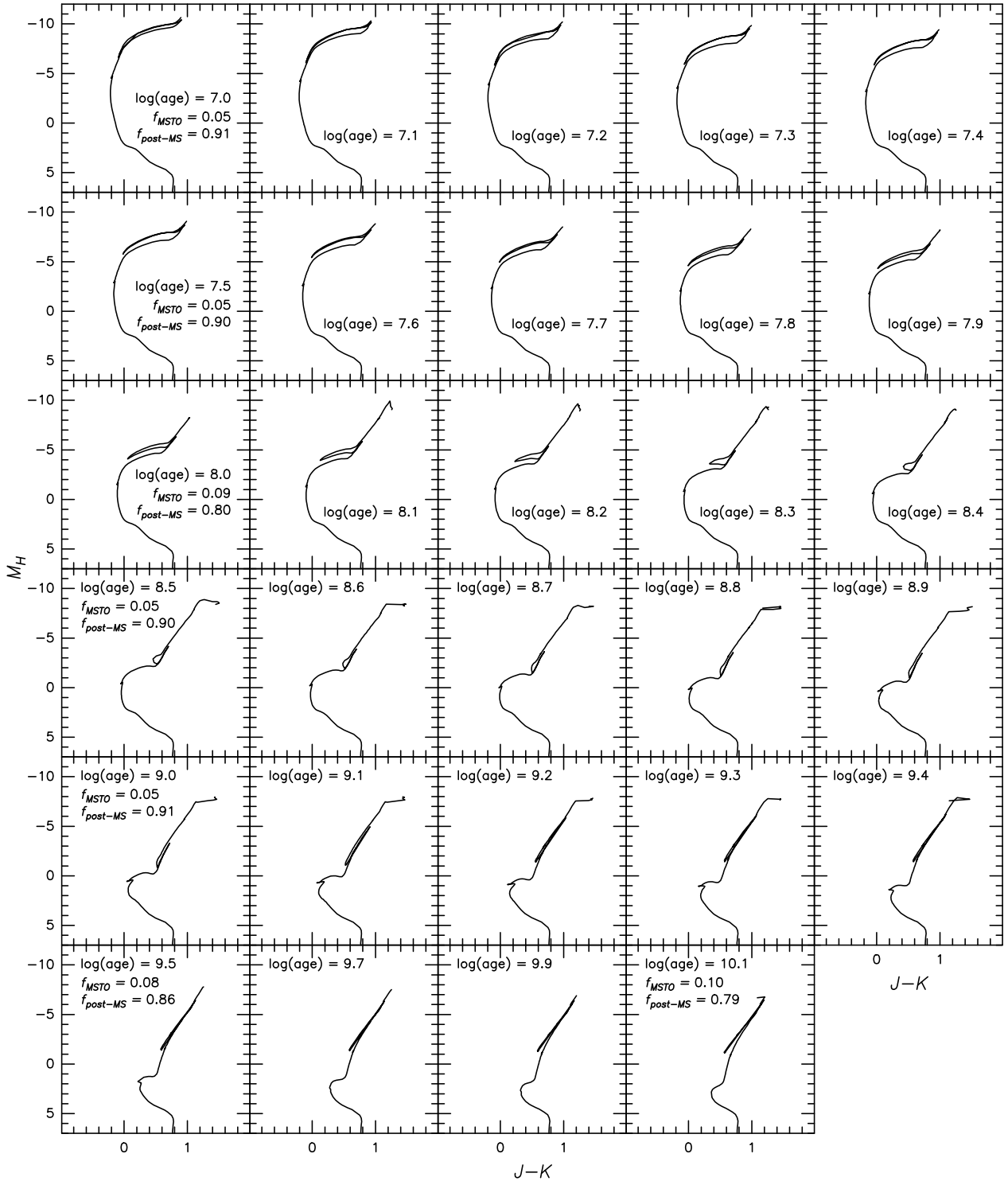


Figure 7. Similar to Figure 5 but now for the NIR range: H vs. $J - K$ CMDs for Padova isochrones with $[Z/H] = -0.4$ and $7.0 \leq \log(\text{age/yr}) \leq 10.1$ (see legend in each panel). Values for f_{MSTO} and $f_{\text{post-MS}}$ now refer to H -band luminosities.

3.2 Red Optical Range: $0.6 - 1.0 \mu\text{m}$

Relative to the blue optical region, the sensitivity of the shape of the integrated-light SED of star clusters to the sampling of high-mass stars in the stellar MF is stronger in the red optical region ($0.6 - 1.0 \mu\text{m}$). This is evident in the right-hand panels of Figure 1 and Figures 2-3, and can be further explained by the shapes of i_{SDSS} vs.

$(r - z)_{\text{SDSS}}$ CMDs of the Padova isochrones (see Figure 6). Comparing the latter with its counterpart for the blue optical region (i.e., Figure 5), it can be seen that the luminosity in the red optical region is significantly more dominated by post-MS stages of stellar evolution, especially the helium-burning stages (e.g., red supergiants or AGB stars) for which the effects of random sampling of the stellar MF are generally strongest. Figure 4 illustrates this in that the de-

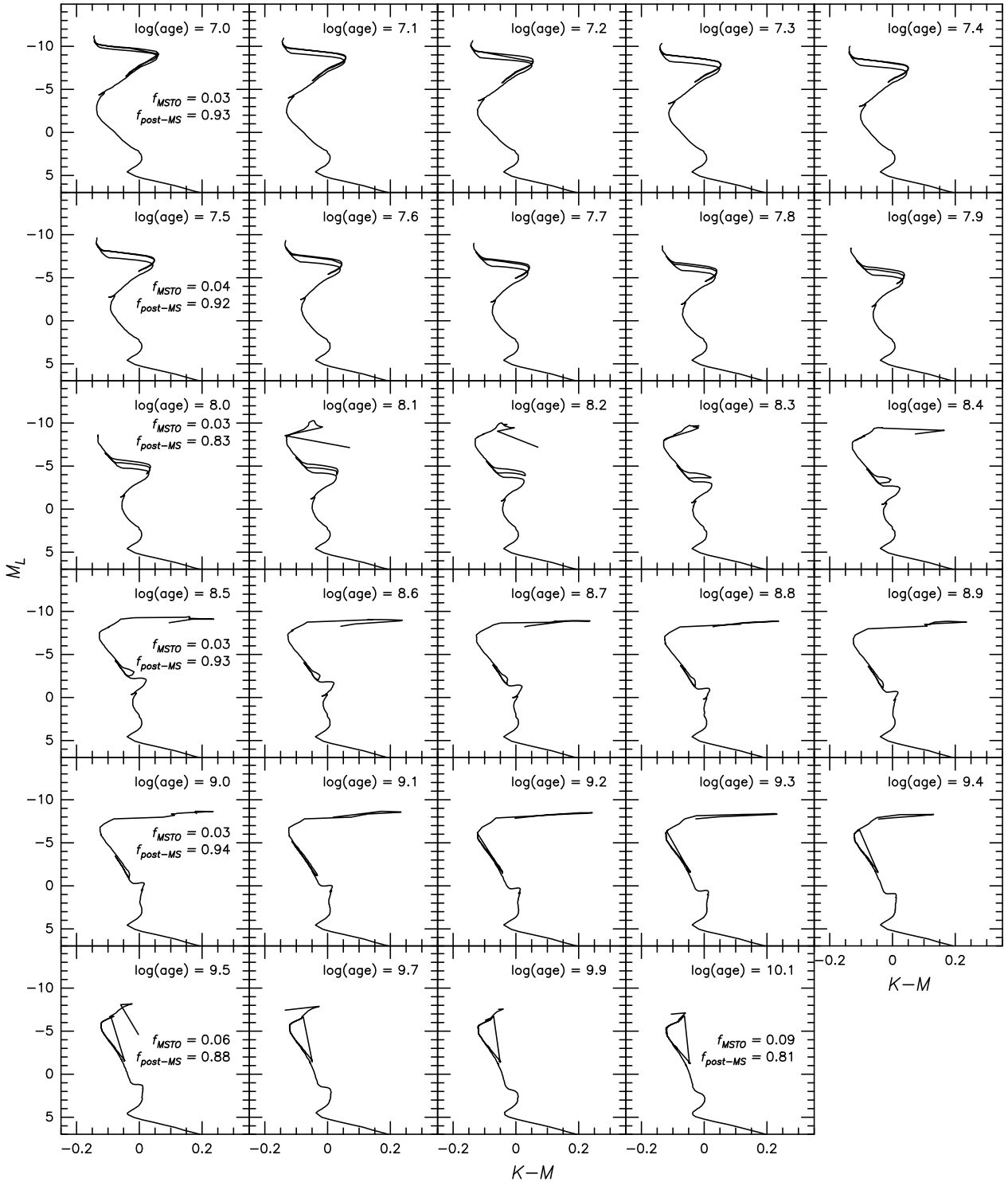


Figure 8. Similar to Figure 5 but now for the mid-IR range: L vs. $K - M$ CMDs for Padova isochrones with $[Z/H] = -0.4$ and $7.0 \leq \log(\text{age/yr}) \leq 10.1$ (see legend in each panel). Values for f_{MSTO} and $f_{\text{post-MS}}$ now refer to L -band luminosities.

viation among SEDs for clusters of $10^4 M_{\odot}$ strongly rises beyond $\lambda \sim 0.7 \mu\text{m}$.

The precision of age and metallicity determination in this wavelength regime as a function of cluster mass is depicted in Figures 11, A3, and A4 (the latter two in the Appendix). We use $\lambda_{\text{norm}} = 9990 \text{ \AA}$ for the full-spectrum fitting in this context.

For a cluster mass of $10^4 M_{\odot}$, we find that the success rate ranges

between just a few % and 70% for $\log(\text{age})$, depending strongly on the age. The success rate for age determination increases with increasing cluster mass, as expected, but the rate of this increase is significantly lower than that seen for the blue optical region in the previous section. The success rate of age determination only reaches close to 100% at a cluster mass of $\sim 3 \times 10^5 M_{\odot}$, and only in the age range of $8.1 \lesssim \log(\text{age/yr}) \lesssim 9.1$. This can be understood by the

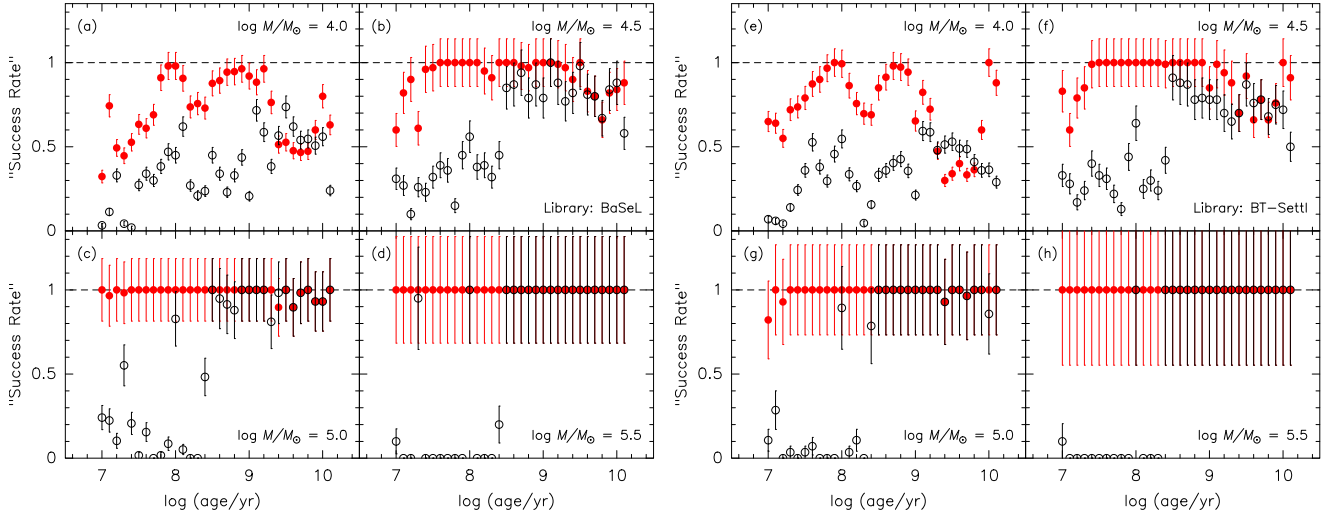


Figure 9. Blue optical range: Percentage of correctly determined $\log(\text{age})$ (solid red circles) and $[Z/H]$ (open black circles) to within 0.1 dex versus $\log(\text{age})$. Error bars represent Poisson uncertainties. Panels (a)–(d) depict results for the BaSeL library for the cluster masses shown in the legend of each panel. Panels (e)–(h) show the same as panels (a)–(d), but now for the BT-Settl library.

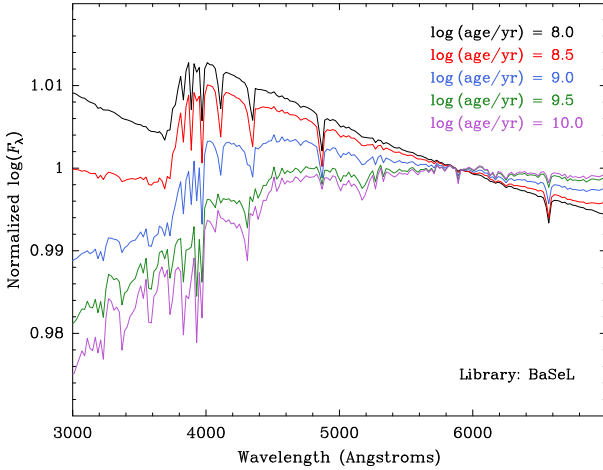


Figure 10. Blue optical SEDs of synthetic SSPs with $[Z/H] = -0.4$. Ages and associated line colours are shown in the legend. The SEDs are normalized to unity at 5870 Å.

shape of SSP SEDs in the red optical region (see Figure 12). For $\log(\text{age}) \lesssim 8.0$, the features in the SEDs are dominated by hydrogen lines ($H\alpha$ and the higher-order Paschen lines), which are produced by hot stars. However, for low-mass clusters, the stochastic fluctuations often cause the hot stars in young clusters not to be dominant in the red optical region (see panel (a) in Figure 4), thus lowering the precision of age determination significantly. For SSPs with $8.1 \lesssim \log(\text{age/yr}) \lesssim 9.1$, the SEDs in the red optical region are dominated by strong molecular bands of TiO due to the large contribution from cool TP-AGB stars, which increases with age in this age interval, thus improving the precision of age determination. The latter then decreases somewhat towards older ages, when the strength of the TiO bands decreases significantly and the main sensitivity to age becomes restricted to the strength of hydrogen lines, which again are produced by the hottest stars in the clusters, whose contribution to the flux in the red optical region depends significantly on stochastic fluctuations at these ages (see panel (f) in Figure 4).

The success rate of metallicity determination in the red optical

range behaves similarly to that of the age determination, both in terms of its overall level and its dependence on cluster mass, except that it typically does not reach beyond $\sim 80\%$ for ages < 100 Myr. This is due in part to the lack of strong metallic spectral features in hot star spectra, especially in this wavelength region (see Figure 12).

Finally, the age and metallicity determination in this regime is on average somewhat better with the BT-Settl library than with the BaSeL one (see Figure 11), especially in case of $[Z/H]$ determination for the lower cluster masses, where the higher spectral resolution helps the identification of the relevant metallic features such as TiO and the Ca II triplet at 8498, 8542, and 8662 Å.

3.3 Near-IR Range: 1.0–2.5 μm

As illustrated by Figures 1–3, the cluster mass has a very strong effect on the level of variations in the shape of the integrated-light SED of the cluster at $\lambda \gtrsim 1 \mu\text{m}$, especially at $\log(\text{age/yr}) \lesssim 7.5$ and $\log(\text{age/yr}) \gtrsim 8.3$. As can be seen in NIR (H vs. $J-K$) CMDs of Padova isochrones (see Figure 7), this is because stars at the top of the stellar MF dominate the NIR luminosity to a greater extent than at shorter wavelengths. The impact of this effect on the precision of age and metallicity determination by full-spectrum fitting in the NIR region are determined by the interplay of the shape and extent of the branch or branches of stars dominating the NIR luminosity, and the relative density of stars within those branches as function of luminosity. The result of this interplay is different in different age ranges, which we discuss and illustrate below in some detail. We use $\lambda_{\text{norm}} = 2.2 \mu\text{m}$ for the full-spectrum fitting in the NIR region, given the lack of significant spectral features on the short- λ side of the first overtone band of CO at $2.3 \mu\text{m}$.

In the youngest clusters (age $\lesssim 30$ Myr), the shape of the SED strongly depends on the distribution of stars along the blue loop of helium-burning stars, which encompasses a relatively large range of T_{eff} . As can be seen in panel (a) in Figure 4, the variety of resulting SEDs causes a wide range of derived best-fit SSP ages and hence a very low success rate for age determination of low-mass clusters in this age range (see Figure 13, and Figures A5 and A6 in the Appendix).

An interesting example of this is illustrated in Figure 14. It shows a

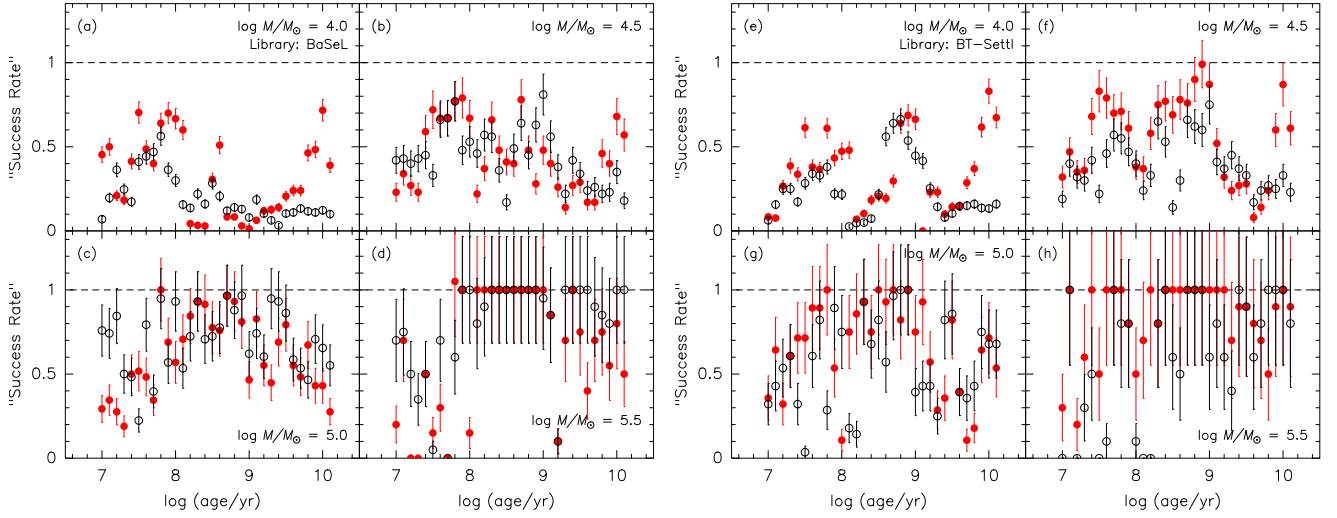


Figure 11. Same as Figure 9, but now for the red optical range.

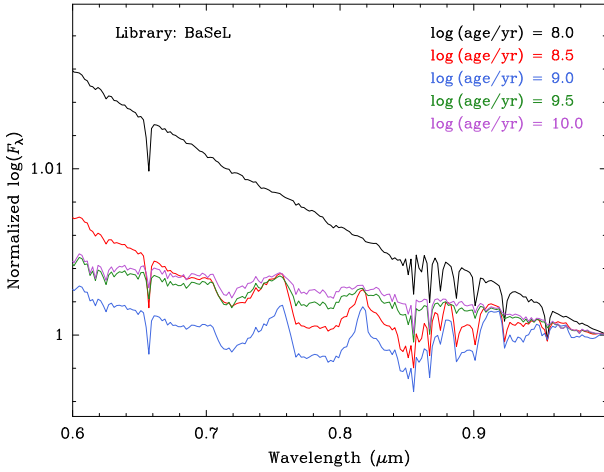


Figure 12. 0.6–1.0 μm SEDs of synthetic SSPs with $[Z/H] = -0.4$. Ages and associated line colours are shown in the legend. The SEDs are normalized to unity at 999 nm. Note the strong molecular bands of TiO at ~ 0.72 , 0.78, 0.85, 0.89, and 0.94 μm for the SSPs with $\log(\text{age/yr}) = 8.5$ and 9.0, when the contribution of TP-AGB stars is largest (see also Lançon & Wood 2000).

M_H vs. $\log T_{\text{eff}}$ diagram² of a simulated $10^4 M_\odot$ cluster with an age of 10 Myr (and $[Z/H] = -0.4$), which happens to have two supergiants at the red (cool) end of the blue loop and one at its blue (hot) end. The lower panel of Figure 14 shows that the NIR SED of that cluster is completely dominated by its two red supergiants, which causes the SED of that cluster to be best fit by an SSP with $(\log(\text{age}), [Z/H]) = (10.1, 0.0)$, thus masquerading as a SSP three orders of magnitude older (and hence also much more massive) than the actual cluster. In strong contrast, the age of this same cluster was recovered correctly to within 0.1 dex in the blue optical regime.

The success rate of age determination increases significantly in the age range of 30–100 Myr, during which increasingly larger percentages of stars populate the “red” branches of shell helium (or hydrogen) burning stars (see Figure 7). This success rate then again

decreases strongly for low-mass clusters at an age of ~ 150 Myr, when the AGB suddenly starts to extend far beyond the blue loop in NIR luminosity, corresponding to the onset of the TP-AGB phase³ (e.g., Marigo et al. 2008). As the luminous TP-AGB is relatively sparsely populated in this age range, stochastic fluctuations have a strong impact. Among low-mass clusters, this causes actual discontinuities in the distribution of integrated NIR and mid-IR fluxes (see panel (d) in Figure 4). However, this trend disappears for higher-mass clusters (see Figure 13), due to their more uniform sampling of the extent of the TP-AGB.

After an age of ~ 600 Myr, the population of stars on the TP-AGB increases with increasing age, which causes the success rate of age determination to increase as well (mainly for the lower-mass clusters). This trend stops at an age of ~ 1 Gyr, when the RGB phase transition occurs and the NIR SED starts to depend critically on the distribution of stars along the AGB and RGB. As an example, for a low cluster mass of $10^4 M_\odot$ and $\log(\text{age/yr}) = 9.1$, our results show that the particular sampling of the RGB and AGB can cause the best-fit SSP $\log(\text{age})$ to vary widely from 7.1 to 9.9 in the NIR regime. Panel (e) in Figure 4 also illustrates the strong effect of stochastic fluctuations around this age.

After the RGB phase transition era, the success rate of age determination gradually increases again with increasing age, due to the increasingly uniform sampling of the RGB and AGB.

In the NIR range, the success rate of metallicity determination as functions of age and cluster mass follows that of the success rate of age determination (see Figures 13, A5, and A6). This is largely due to the strong and wide molecular bands of H_2O at ~ 1.4 and 1.9 μm which are only produced by the coolest TP-AGB stars that provide a significant fraction of the NIR flux in the age range of $8.5 \lesssim \log(\text{age/yr}) \lesssim 9.2$. This is illustrated in Figure 15 and further discussed in the next Section.

Finally, Figure 13 shows that BaSeL and BT-Settl libraries generally yield similar success rates of age and metallicity determination in the NIR regime. The only qualitative difference between the two is that the higher spectral resolution of the BT-Settl library provides

² We chose $\log T_{\text{eff}}$ for the abscissa to maximize the resolution of the stars’ sampling of the isochrone.

³ This phase in stellar evolution is sometimes referred to as the “AGB phase transition” (see, e.g., Renzini & Buzzoni 1986; Maraston 2005).

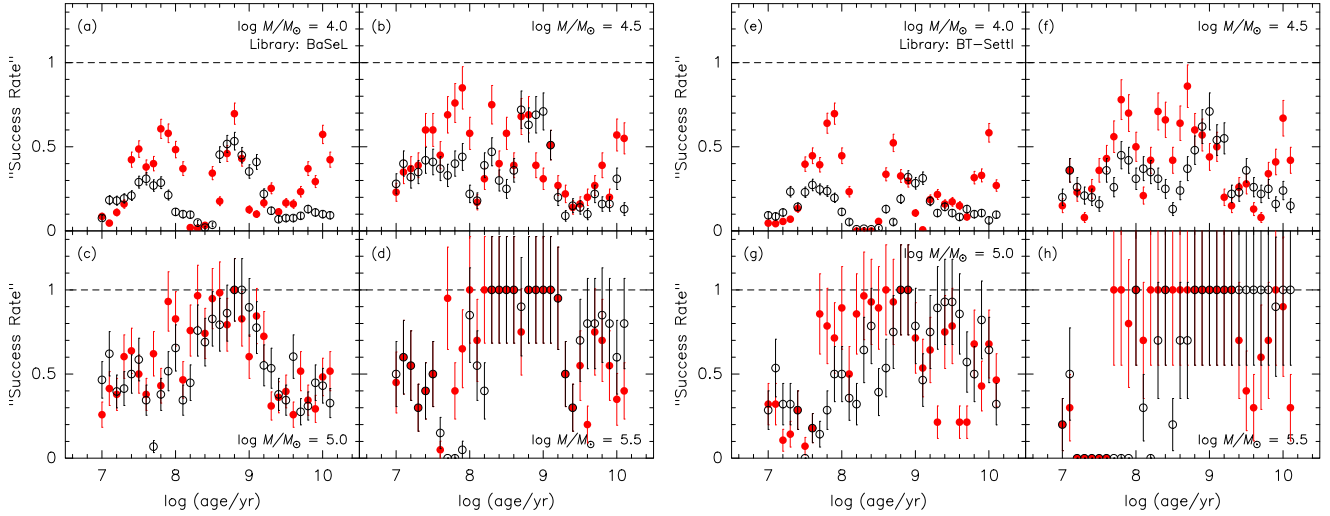


Figure 13. Same as Figure 9, but now for the NIR range.

somewhat better metallicity determination for massive clusters with older ages ($\gtrsim 2$ Gyr).

3.4 Mid-IR Range: 2.5–5.0 μm

In the mid-IR regime, the post-MS stages of stellar evolution contribute the highest luminosity fraction in this regime relative to those at shorter wavelengths (see Figure 8). As such, stochastic fluctuations have a large impact on the *luminosities* of low-mass star clusters in the mid-IR regime. However, the spectral radiance of electromagnetic radiation in the mid-IR is well approximated by the Rayleigh-Jeans law, and as such, the shapes of SEDs of SSPs of different ages, as well as SEDs of different clusters of a given mass, generally look more similar to one another than at shorter wavelengths (see Figure 4).

The shape of isochrone CMDs in the mid-IR, shown in Figure 8, emphasizes this in that differences in $K - M$ colour between the various phases of stellar evolution stay within ~ 0.3 mag. The overall similarity of shapes of mid-IR CMDs of isochrones of young ($\lesssim 300$ Myr) and old ($\gtrsim 3$ Gyr) SSPs is especially remarkable.

However, in the age range considered here, there is one phase of stellar evolution with a recognizable impact to shapes of mid-IR SEDs. This is the TP-AGB, which dominates the mid-IR luminosity in the age range of $8.5 \leq \log(\text{age/yr}) \leq 9.2$. It extends to effective temperatures that are even lower than the low-mass end of the MS. In our synthetic SSP SEDs, the main spectral features caused by the cool TP-AGB stars are (1) wide and relatively strong H_2O bands at ~ 1.4 , 1.9 , and $2.8 \mu\text{m}$ ⁴, and (2) an excess of continuum radiation beyond the $\sim 2.8 \mu\text{m}$ band of H_2O relative to SSPs with younger or older ages (see Figure 15). With this in mind, we use $\lambda_{\text{norm}} = 3.5 \mu\text{m}$ for full-spectrum fitting in the mid-IR regime.

The H_2O bands mentioned above are intrinsically strong, especially the $2.8 \mu\text{m}$ band, which is the strongest spectral absorption feature in the 2.5–5 μm mid-IR range when the physical environment is conducive to the formation of H_2O bands. And indeed, the success rate of metallicity determination using full-spectrum fitting

in the mid-IR as functions of age and cluster mass follows that of the success rate of age determination. In fact, it does so even more closely than in the NIR (see Figure 16, and Figures A7 and A8 in the Appendix). This is likely due to the fundamental (1-0) CO bandhead at $4.6 \mu\text{m}$, which is stronger than the first overtone CO bandhead at $2.3 \mu\text{m}$.

In terms of the impact of different spectral resolutions, Figure 16 shows that the use of the BaSeL vs. BT-Settl libraries does not translate in any significant differences in the success rate of age and metallicity determination (as defined in Section 3.1) in the mid-IR regime. However, a comparison of Figures A7 and A8 shows that the higher spectral resolution of the BT-Settl library does translate in a significant improvement in terms of the accuracy and precision of age determination at ages $\gtrsim 2$ Gyr. Specifically, the use of the BaSeL library causes a bimodal distribution of the fitted age for those ages, which does not occur for the BT-Settl library. To understand this difference, we compare SSP SEDs in the 2–5 μm region after normalizing by the SED for an age of 10 Gyr in Figure 17. It can be seen that the aforementioned difference is due, at least in part, to narrow spectral features such as the Brackett and Pfund series of Hydrogen that occur in hot stars in young SSPs, which are smoothed over by the low resolution of the BaSeL library. Note however that these intrinsic differences between “young” and “old” SSP SEDs in the mid-IR regime are only at the % level. Hence, detection of these differences in observed spectra will require relatively high signal-to-noise (S/N) ratios. On the other hand, the M/L ratio in the mid-IR regime for a SSP with an age of 10 Gyr is factors $\sim 7 - 45$ higher than for SSPs with ages between 10 and 100 Myr (see Figure 18), thus rendering a detection of a luminous cluster in the mid-IR to be much more likely to be young rather than old.

3.5 The cluster mass dependence of age and [Z/H] recovery in different wavelength regimes

Using the results described above in Sections 3.1–3.4, we illustrate the cluster mass dependence of the success rate of age and metallicity determination in the various wavelength regimes in Figures 19 and 20, while Figures 21 and 22 show the cluster mass dependence of the mean offset and standard deviation of derived $\log(\text{age})$ and $[\text{Z}/\text{H}]$ from the true values. To avoid overcrowding the plots, the results are only shown for $7.0 \leq \log(\text{age/yr}) \leq 10.0$ with a step size of

⁴ We recall that we model TP-AGB stars as oxygen-rich M stars. However, if instead the TP-AGB happens to be dominated by carbon stars in a given cluster in this age range, then the SED will have equally recognizable features from CN, C_2 , HCN, and C_2H_2 in the 1–5 μm region (Aringer et al. 2009).

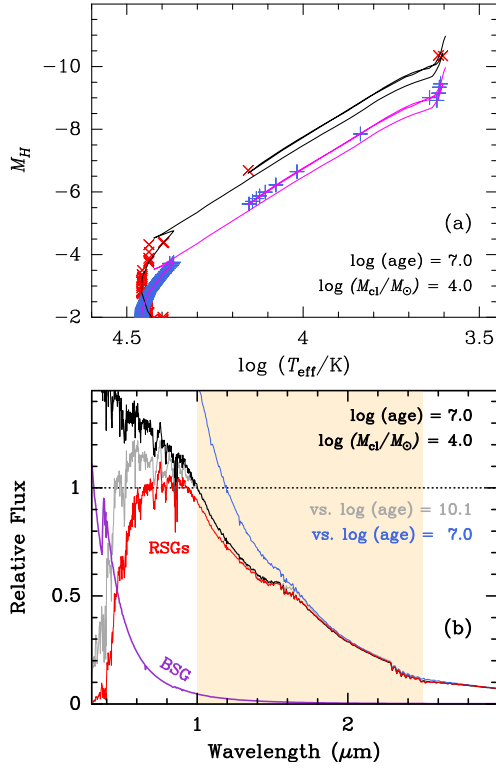


Figure 14. Illustration of simulated $10^4 M_{\odot}$ cluster with $\log(\text{age/yr}) = 7.0$ masquerading as an SSP with $\log(\text{age/yr}) = 10.1$ in the NIR. *Panel (a):* M_H vs. $\log T_{\text{eff}}$ diagram. The solid black line depicts the Padova isochrone with $(\log(\text{age/yr}), [Z/H]) = (7.0, -0.4)$. Red crosses represent stars in simulated cluster #111. For comparison, the magenta line shows the same isochrone, offset by +1.0 mag in M_H for clarity purposes, while the blue plus signs represent points along that isochrone for a regular grid of initial masses ($\Delta M_i = 0.08$ in this case) to represent a uniform mass sampling cadence equivalent to a full IMF sampling. Note the two bright red supergiants in cluster #111, with only one counterpart at the blue end of the blue loop. *Panel (b):* the black line represents the integrated spectrum of cluster #111, normalized to unity at $\lambda = 1 \mu\text{m}$. The red line represents the co-added spectra of the two red supergiants shown in panel (a), using the same normalization factor. For comparison, the purple line represents the spectrum of the blue supergiant in cluster #111. Finally, the blue and grey lines represent spectra for SSPs with $(\log(\text{age}), [Z/H]) = (7.0, -0.4)$ and $(10.1, 0.0)$, respectively, normalized to fit the flux of cluster #111 at $\lambda = 2.2 \mu\text{m}$. Note that the NIR spectrum of cluster #111 is dominated by its red supergiants, and fit much better by a $\log(\text{age}) = 10.1$ SSP spectrum than by that of its own $\log(\text{age}) = 7.0$.

0.5 dex. These Figures allow a quick comparison of the power of the various wavelength regimes, not just in terms of the cluster mass dependence of the accuracy and precision of age and metallicity determination, but also in terms of the identification of certain types of populations through full-spectrum fitting. For example, if the goal is to identify young massive clusters (YMCs, with ages $\lesssim 100$ Myr and masses $\gtrsim 10^5 M_{\odot}$) in distant galaxies, Figures 19–22 show that while the blue optical range is in principle best suited for that goal, the mid-IR range is a good alternative (and actually better than the blue optical range in terms of $[Z/H]$ measurement precision, due to the strong CO (1-0) bandhead at $4.6 \mu\text{m}$). Moreover, star forming regions typically exhibit high and non-uniform extinction, and extinction in the mid-IR is factors $\gtrsim 10^4$ lower than in the blue optical range, thus allowing surveys that are significantly less impacted by regions of high extinction. This is illustrated in Figure 23

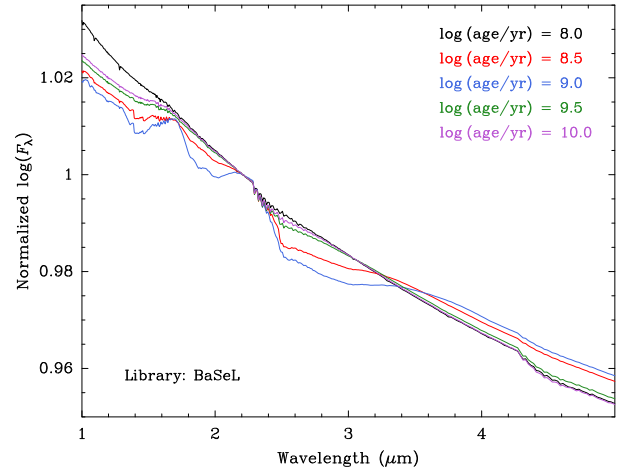


Figure 15. 1–5 μm SEDs of synthetic SSPs with $[Z/H] = -0.4$. Ages and associated line colours are shown in the legend. The SEDs are normalized to unity at $2.2 \mu\text{m}$. Note the strong H_2O bands at $\sim 1.4, 1.9$, and $2.8 \mu\text{m}$ along with an excess of continuum radiation beyond the $2.8 \mu\text{m}$ band for the SSPs with $\log(\text{age/yr}) = 8.5$ and 9.0 , when the contribution of cool TP-AGB stars is largest.

for an SSP with $\log(\text{age/yr}) = 7.5$ and an extinction $A_V = 10$ mag, which is not untypical for YMCs detected in optical images of star-forming galaxies (e.g., Wilson et al. 2006). Finally, we note that the omission of the influence of circumstellar dust around upper AGB stars in our modeling (cf. Section 2.1.2) is not expected to have an impact on this result, since AGB stars with circumstellar dust shells only start having a significant contribution to the integrated mid-IR light at an age of about 200 Myr, after the YMC era (see, e.g., Villaume et al. 2015).

4 SUMMARY

We studied the effects of stochastic fluctuations of stellar masses near the top of the stellar mass function in star clusters as a function of the star cluster mass in terms of variations of SSP-equivalent ages and metallicities derived using the technique of full-spectrum fitting, and how the level of those variations depends on star cluster mass (in the range of $10^4 \leq M/M_{\odot} < 10^6$) and wavelength (in the range of $0.3 \leq \lambda/\mu\text{m} \leq 5$). To this end, we created a large set of simulated star cluster spectra which we compared with simulated “true” SSP spectra, using the same isochrones and spectral libraries. The age range considered in our study is $7.0 \leq \log(\text{age/yr}) \leq 10.1$. We also compared the results when using two different spectral libraries (BaSeL and BT-Settl), featuring different physical model ingredients and spectral resolutions. We analyzed four different spectral regimes: blue optical ($0.35\text{--}0.7 \mu\text{m}$), red optical ($0.6\text{--}1.0 \mu\text{m}$), near-IR ($1.0\text{--}2.5 \mu\text{m}$), and mid-IR ($2.5\text{--}5.0 \mu\text{m}$). The results can be summarized as follows.

- In general, the blue optical regime ($0.35\text{--}0.7 \mu\text{m}$) is by far the least impacted by stochastic fluctuations among the wavelength regimes studied here. This is reflected in it yielding the highest accuracy and precision of age determination (for clusters of all ages) and metallicity determination (for ages $\gtrsim 300$ Myr). With the exception of the youngest clusters in our simulations ($\log(\text{age/yr}) \lesssim 7.5$), the full precision of age and metallicity determination through full-spectrum fitting in the blue optical regime is already reached at a cluster mass of $\sim 3 \times 10^4 M_{\odot}$, which is a factor $\gtrsim 10$ lower

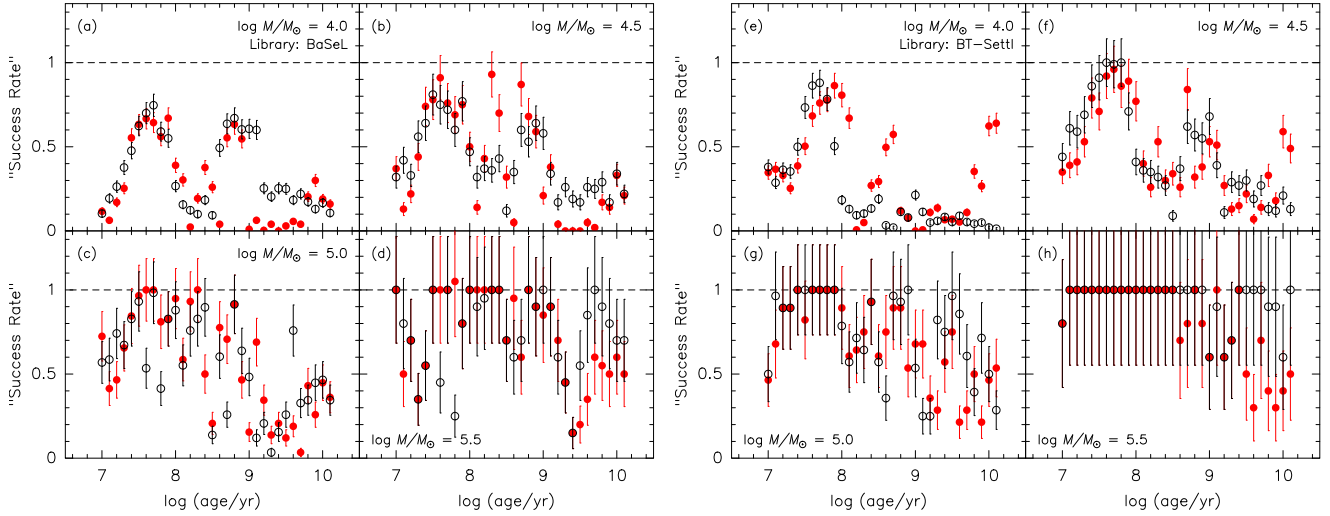


Figure 16. Same as Figure 9, but now for the mid-IR range.

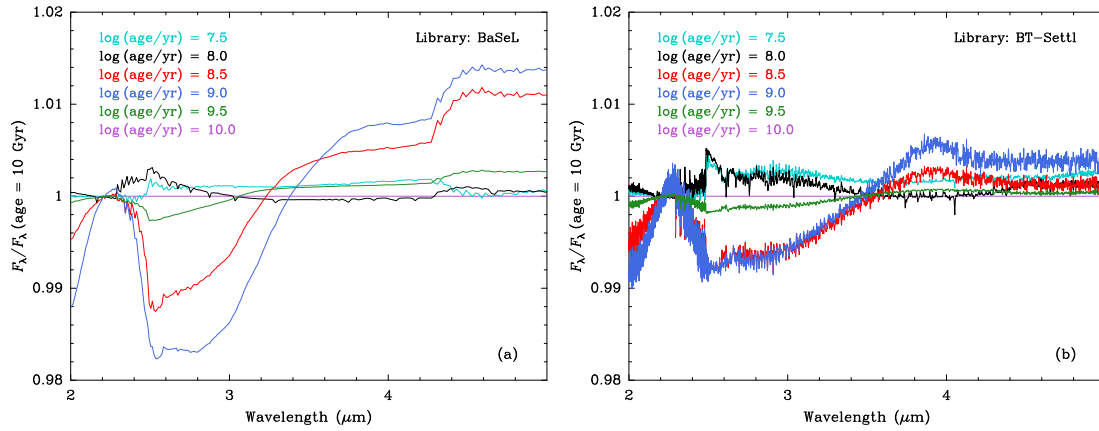


Figure 17. 2–5 μm flux ratios of SEDs of SSPs relative to that of a SSP with an age of 10 Gyr. The SED curves are normalized to unity at 2.2 μm to highlight shape differences. Different line colours correspond to different ages as shown in the legend. All SSPs shown have $[Z/H] = -0.4$. Panel (a) shows the ratios for the BaSeL spectral library while panel (b) does so for the BT-Settl library. See discussion in Section 3.4.

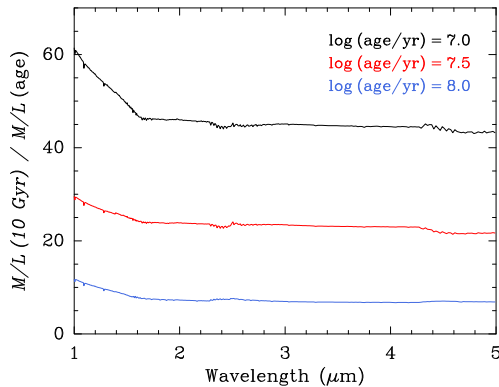


Figure 18. M/L in the 1–5 μm region of a 10-Gyr-old SSP relative to those of SSPs of ages 10 Myr, 30 Myr, and 100 Myr (see legend), using the BaSeL library. See discussion in Section 3.4.

than for all other wavelength regimes (with $\lambda > 0.6 \mu\text{m}$) studied here. However, metallicity determination for SSPs with $\log(\text{age/yr}) \lesssim 8.5$ suffers from significant systematic errors (of order $\lesssim 0.5$ dex)

in this regime. These findings are similar for the BaSeL and BT-Settl spectral libraries.

- The red optical regime (0.6–1.0 μm) and the near-IR regime (1.0–2.5 μm) have similar power in terms of their accuracy and precision of age and metallicity determination using full-spectrum fitting. The impact of stochastic fluctuations is large across virtually all ages in these wavelength regimes, leading to errors that can reach beyond 2 dex in age and beyond 0.5 dex in $[Z/H]$ for clusters with $M/M_\odot < 10^5$, depending on the age. The largest cluster mass dependence of the precision of age determination is found around the ages where the luminous TP-AGB or RGB stages start to be populated (i.e., $\log(\text{age/yr}) \sim 8.4$ and 9.0, respectively), especially in the NIR regime. The choice of spectral library (BaSeL vs. BT-Settl) has little impact on our findings in the red optical and NIR regimes.

- Stochastic fluctuations also have a large impact on the luminosities of star clusters in the mid-IR regime (2.5–5.0 μm). This is because the post-MS stages of stellar evolution contribute the highest luminosity fraction in this regime relative to those at shorter wavelengths. However, with the important exception of clusters older than ≈ 2 Gyr (see below), these fluctuations in luminosity do not generally cause significant inaccuracy of age determination in the mid-IR

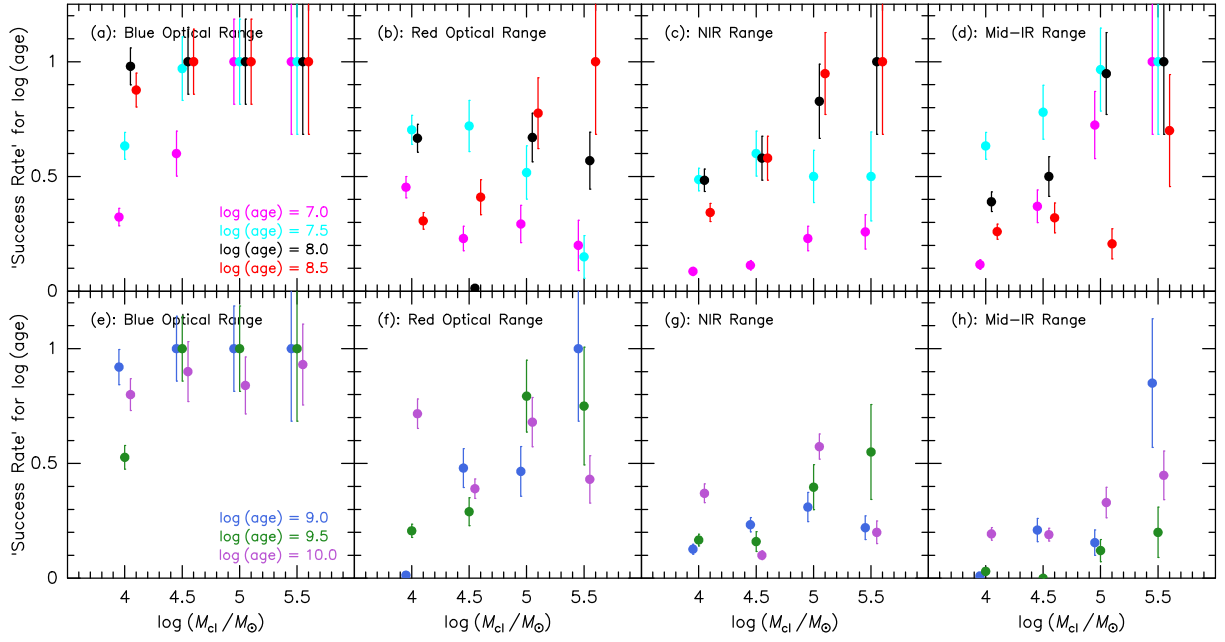


Figure 19. Success rate of age determination as a function of cluster mass M_{cl} , for the four wavelength regimes discussed in this paper: blue optical range (panels a and e), red optical range (panels b and f), NIR range (panels c and g), and mid-IR (panels d and h). Different ages are indicated by different symbol colours (see legend in panels a and e). To improve clarity, the symbols for different ages within a given panel are slightly offset in $\log(M_{\text{cl}})$ from one another (by $\Delta \log(M_{\text{cl}}) = 0.05$).

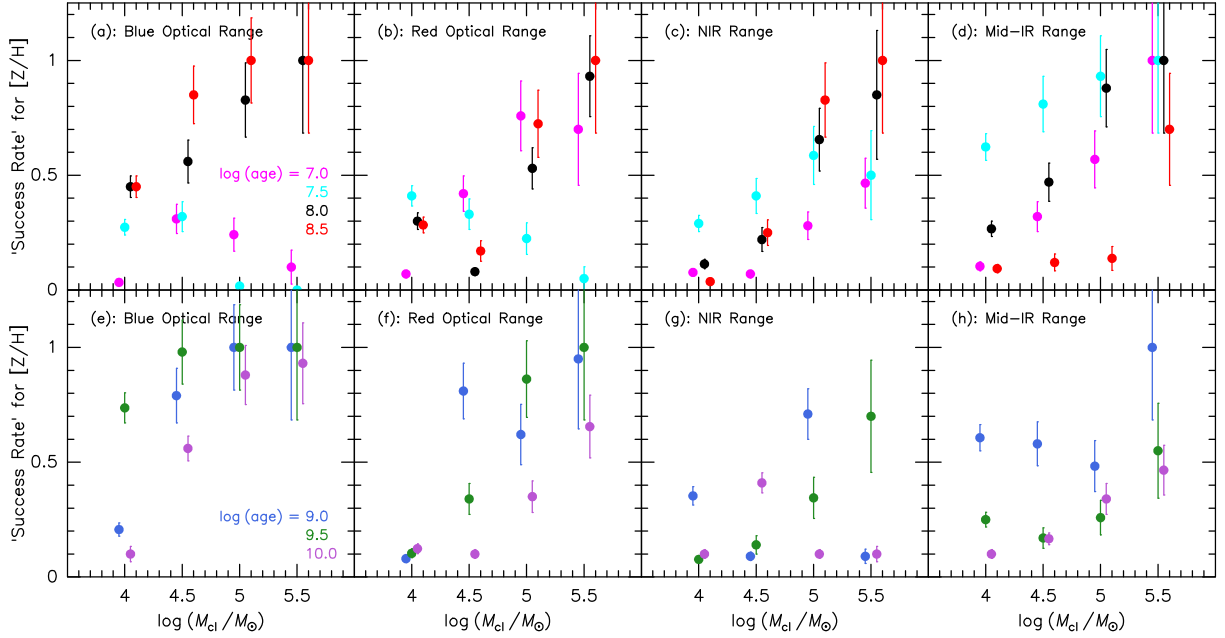


Figure 20. Similar to Figure 19, but now plotting the success rate of $[Z/H]$ determination. Symbols are the same as in Figure 19.

regime. For the age range in which the TP-AGB provides a significant contribution to the luminosity, this is caused by two features that clearly identify this stage: a strong H_2O band at $2.8 \mu\text{m}$ and a significant excess of continuum radiation at $\lambda \gtrsim 3 \mu\text{m}$ due to the cool TP-AGB stars. However, the mid-IR SEDs of SSPs with age $\gtrsim 2$ Gyr are generally very similar to those with age $\lesssim 100$ Myr. Use of the low-resolution BaSeL spectral library causes this to yield an approximately bimodal distribution of best-fit ages for old clusters, especially for those with $M/M_{\odot} \leq 10^5$. This bimodality disappears

when using the higher-resolution BT-Settl library, and it also does not occur for young clusters in our tests.

In fact, we find the mid-IR to be a powerful regime for the purpose of surveying and identifying young massive clusters in star-forming regions. While its accuracy and precision of age determination for ages $\lesssim 600$ Myr is slightly below that of the blue optical region, the mid-IR is significantly less impacted by the strong extinction that is common in star-forming regions.

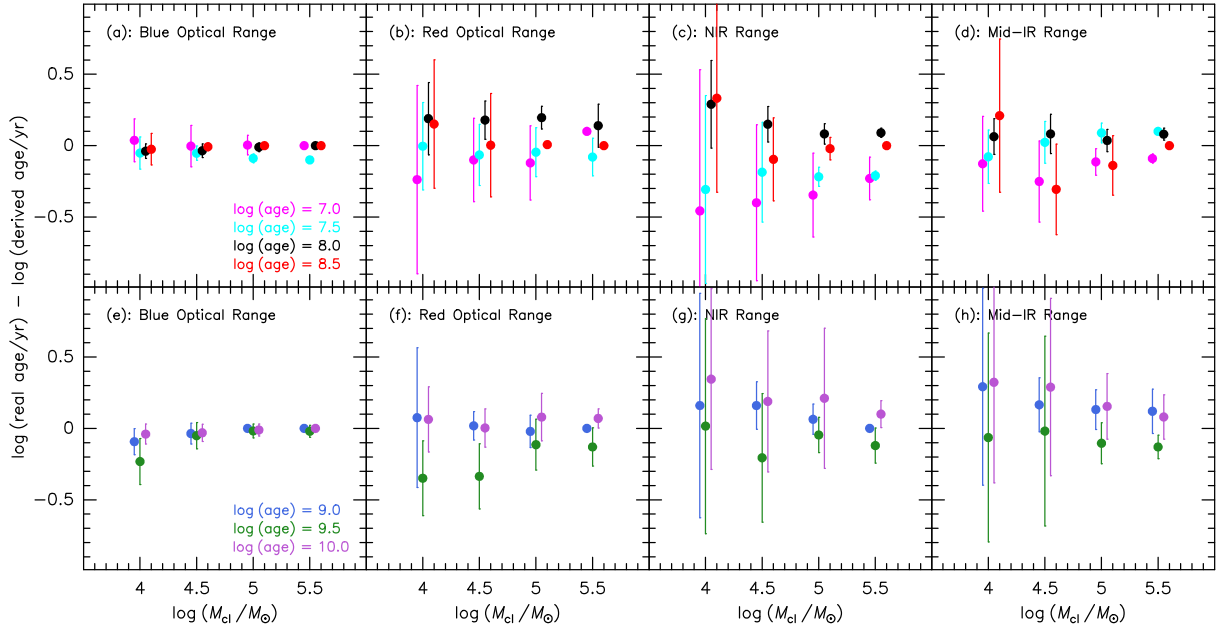


Figure 21. Similar to Figure 19, but now plotting the mean offset of the best-fit $\log(\text{age})$ from the true value along with its standard deviation among the simulated clusters. Symbols are the same as in Figure 19.

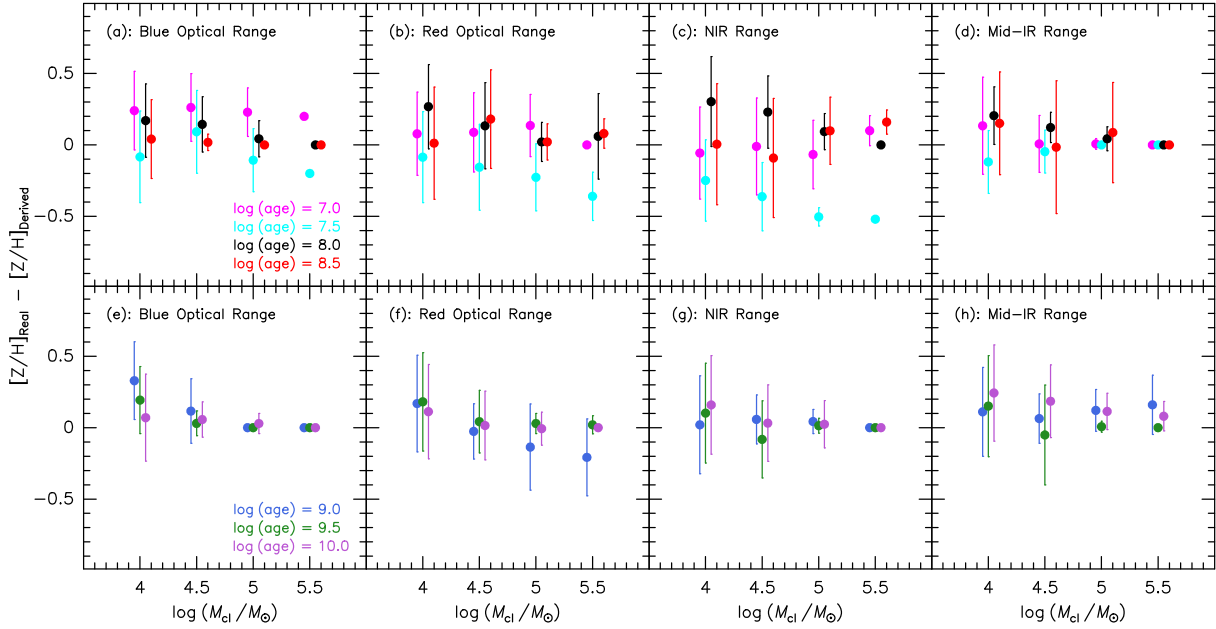


Figure 22. Similar to Figure 19, but now plotting the mean offset of the best-fit $[Z/H]$ from the true value along with its standard deviation among the simulated clusters. Symbols are the same as in Figure 19.

ACKNOWLEDGMENTS

We thank Morgan Fouesneau for providing us access to the high-resolution BT-Settl spectral library as an add-on to his `pystel-libs` GitHub repository. RA thanks the Space Telescope Science Institute for a sabbatical visitorship including travel and subsistence support as well as access to their science cluster computer facilities. We acknowledge use of the software packages NumPy (Oliphant 2006), AstroPy (Astropy Collaboration et al. 2013; Price-Whelan et al. 2018), Matplotlib (Hunter 2007), and Gildas (<https://www.iram.fr/IRAMFR/GILDAS>).

DATA AVAILABILITY

The model spectra of all mock star clusters and SSPs created for this paper are available through the [website of the corresponding author](#). They will also be made available through CDS once this paper gets a formal MNRAS reference.

REFERENCES

Allard F., Homeier D., Freytag B., 2012, *Philosophical Transactions of the*

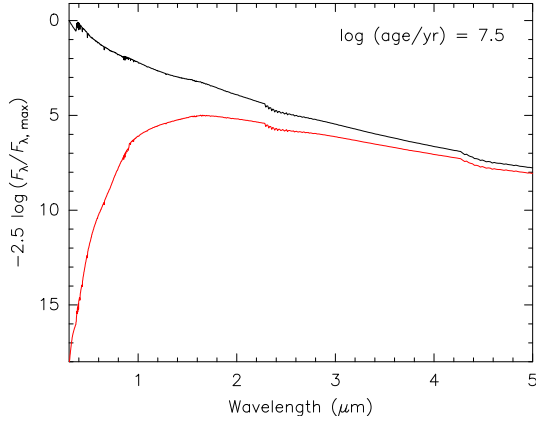


Figure 23. The black line represents the 0.3–5 μm SED of a SSP with $\log(\text{age/yr}) = 7.5$ in magnitude flux units, normalized to 0 at the wavelength of maximum flux. The red line represents the same SED after applying $A_V = 10$ mag of extinction using the Cardelli et al. (1989) prescription for $R_V = 3.1$.

Royal Society of London Series A, 370, 2765
 Aringer B., Girardi L., Nowotny W., Marigo P., Lederer M. T., 2009, *A&A*, 503, 913
 Asa'd R. S., 2014, *MNRAS*, 445, 1679
 Asa'd R., Goudfrooij P., 2020, *MNRAS*, 498, 2814
 Asa'd R. S., Hanson M. M., Ahumada A. V., 2013, *PASP*, 125, 1304
 Asa'd R. S., Vazdekis A., Zeinelabdin S., 2016, *MNRAS*, 457, 2151
 Astropy Collaboration et al., 2013, *A&A*, 558, A33
 Bastian N., Lardo C., 2018, *ARA&A*, 56, 83
 Benítez-Llambay A., Clariá J. J., Piatti A. E., 2012, *PASP*, 124, 173
 Bica E., Alloin D., 1986, *A&A*, 162, 21
 Boyer M. L., et al., 2019, *ApJ*, 879, 109
 Brodie J. P., Strader J., 2006, *ARA&A*, 44, 193
 Brown T. M., et al., 2016, *ApJ*, 822, 44
 Cardelli J. A., Clayton G. C., Mathis J. S., 1989, *ApJ*, 345, 245
 Cerviño M., Luridiana V., 2004, *A&A*, 413, 145
 Cerviño M., Luridiana V., 2006, *A&A*, 451, 475
 Chandar R., Fall S. M., Whitmore B. C., 2010, *ApJ*, 711, 1263
 Chilingarian I. V., Asa'd R., 2018, *ApJ*, 858, 63
 Cid Fernandes R., Gonzalez Delgado R. M., 2010, *MNRAS*, 403, 780
 Cioni M. R. L., Habing H. J., 2005, *A&A*, 429, 837
 Conroy C., Gunn J. E., White M., 2009, *ApJ*, 699, 486
 Fall S. M., Chandar R., Whitmore B. C., 2009, *ApJ*, 704, 453
 Fouesneau M., Lançon A., 2010, *A&A*, 521, A22
 Fouesneau M., Lançon A., Chandar R., Whitmore B. C., 2012, *ApJ*, 750, 60
 Fouesneau M., et al., 2014, *ApJ*, 786, 117
 Girardi L., Bica E., 1993, *A&A*, 274, 279
 Goudfrooij P., 2012, *ApJ*, 750, 140
 Goudfrooij P., 2018, *ApJ*, 857, 16
 Goudfrooij P., Schweizer F., Gilmore D., Whitmore B. C., 2007, *AJ*, 133, 2737
 Goudfrooij P., Puzia T. H., Kozhurina-Platais V., Chandar R., 2009, *AJ*, 137, 4988
 Goudfrooij P., Puzia T. H., Kozhurina-Platais V., Chandar R., 2011, *ApJ*, 737, 3
 Greggio L., Renzini A., 1990, *ApJ*, 364, 35
 Hunter J. D., 2007, *Computing in Science & Engineering*, 9, 90
 Kroupa P., 2001, *MNRAS*, 322, 231
 Krumholz M. R., Fumagalli M., da Silva R. L., Rendahl T., Parra J., 2015, *MNRAS*, 452, 1447
 Krumholz M. R., Adamo A., Fumagalli M., Calzetti D., 2019, *MNRAS*, 482, 3550
 Lada C. J., Lada E. A., 2003, *ARA&A*, 41, 57
 Lançon A., Mouhcine M., 2000, in Lançon A., Boily C. M., eds, *Astronom-*

ical Society of the Pacific Conference Series Vol. 211, Massive Stellar Clusters, p. 34 ([arXiv:astro-ph/0003451](https://arxiv.org/abs/astro-ph/0003451))
 Lançon A., Mouhcine M., 2002, *A&A*, 393, 167
 Lançon A., Wood P. R., 2000, *A&AS*, 146, 217
 Lee H.-C., Yoon S.-J., Lee Y.-W., 2000, *AJ*, 120, 998
 Lejeune T., Cuisinier F., Buser R., 1998, *A&AS*, 130, 65
 Maraston C., 2005, *MNRAS*, 362, 799
 Maraston C., Thomas D., 2000, *ApJ*, 541, 126
 Maraston C., Greggio L., Renzini A., Ortolani S., Saglia R. P., Puzia T. H., Kissler-Patig M., 2003, *A&A*, 400, 823
 Marigo P., Girardi L., Bressan A., Groenewegen M. A. T., Silva L., Granato G. L., 2008, *A&A*, 482, 883
 Martocchia S., et al., 2018, *MNRAS*, 477, 4696
 Milone A. P., et al., 2018, *MNRAS*, 481, 5098
 Oliphant T. E., 2006, *A guide to NumPy*, Vol. 1, Trelgol Publishing USA
 Piskunov A. E., Kharchenko N. V., Schilbach E., Röser S., Scholz R. D., Zinnecker H., 2009, *A&A*, 507, L5
 Popescu B., Hanson M. M., 2009, *AJ*, 138, 1724
 Popescu B., Hanson M. M., 2010a, *ApJ*, 713, L21
 Popescu B., Hanson M. M., 2010b, *ApJ*, 724, 296
 Popescu B., Hanson M. M., Elmegreen B. G., 2012, *ApJ*, 751, 122
 Price-Whelan A. M., et al., 2018, *AJ*, 156, 123
 Renzini A., Buzzoni A., 1986, *Global properties of stellar populations and the spectral evolution of galaxies..* pp 195–231, doi:10.1007/978-94-009-4598-2_19
 Sánchez-Blázquez P., Ocvirk P., Gibson B. K., Pérez I., Peletier R. F., 2011, *MNRAS*, 415, 709
 Santos J. F. C. J., Frogel J. A., 1997, *ApJ*, 479, 764
 Santos Jr. J. F. C., Bica E., Claria J. J., Piatti A. E., Girardi L. A., Dottori H., 1995, *MNRAS*, 276, 1155
 Santos J. F. C., Claria J. J., Ahumada A. V., Bica E., Piatti A. E., Parisi M. C., 2006, *A&A*, 448, 1023
 Schiavon R. P., 2007, *ApJS*, 171, 146
 Schiavon R. P., Caldwell N., Rose J. A., 2004, *The Astronomical Journal*, 127, 1513
 Trager S. C., Worthey G., Faber S. M., Dressler A., 2005, *MNRAS*, 362, 2
 Villaume A., Conroy C., Johnson B. D., 2015, *ApJ*, 806, 82
 Wilkinson D. M., Maraston C., Goddard D., Thomas D., Parikh T., 2017, *MNRAS*, 472, 4297
 Wilson C. D., Harris W. E., Longden R., Scoville N. Z., 2006, *ApJ*, 641, 763
 Worthey G., 1994, *ApJS*, 95, 107

APPENDIX A: PLOTS OF THE DISTRIBUTION OF SSP FITTING RESULTS

In this appendix, we show plots of the full distributions the differences of the ages and metallicities of all simulated clusters found through full-spectrum fitting with respect to the "true" input values. These distributions are shown as a function of input age, and separately for each wavelength regime discussed in this paper.

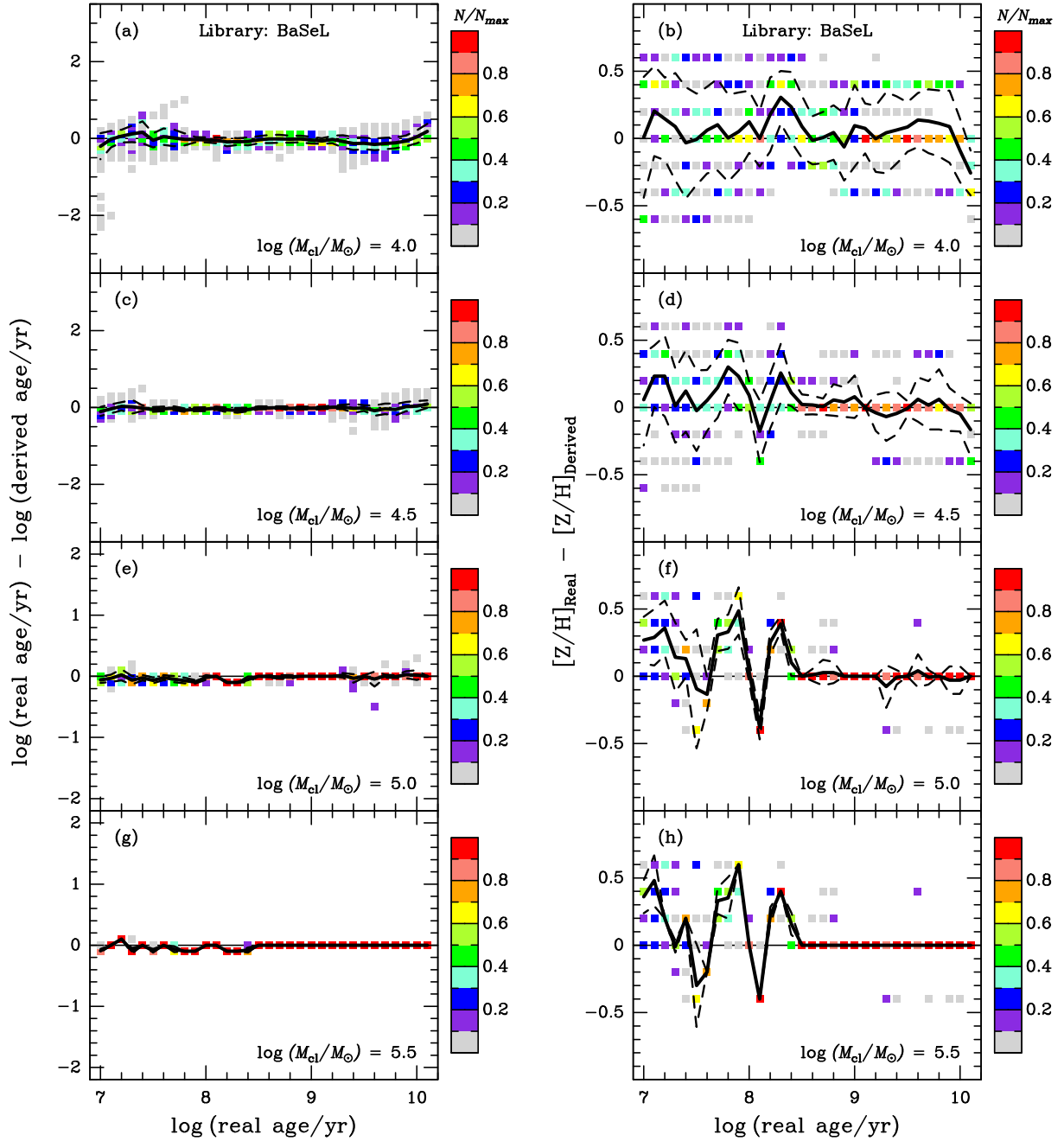


Figure A1. Blue optical range: SSP fitting results for age (left panels) and $[Z/H]$ (right panels) expressed as offsets of the best fit in $\log(\text{age})$ or $[Z/H]$ from the true value, as a function of $\log(\text{age})$. The symbol colour indicates the relative number of times that offset occurred in the results (see colour bar on the right side of each panel). Different rows of panels show the results for different cluster masses M_{cl} (see legends). The thick black solid line in each panel indicates the average offset, and the two dashed lines indicate $\pm 1\sigma$ from the average offset. The BaSeL spectral library is used for the results in this Figure.

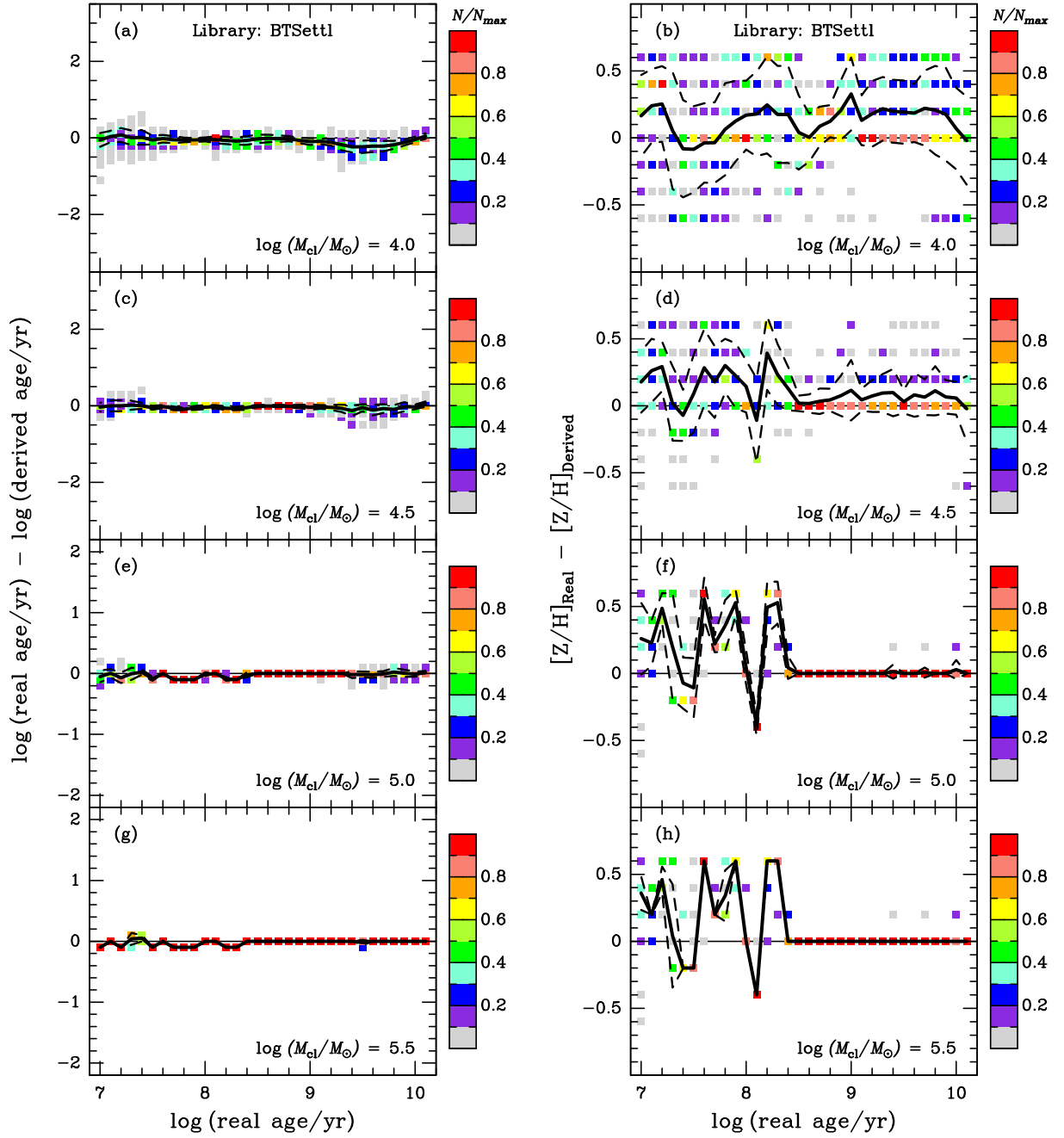


Figure A2. Similar to Figure A1, but now using the BT-Settl library.

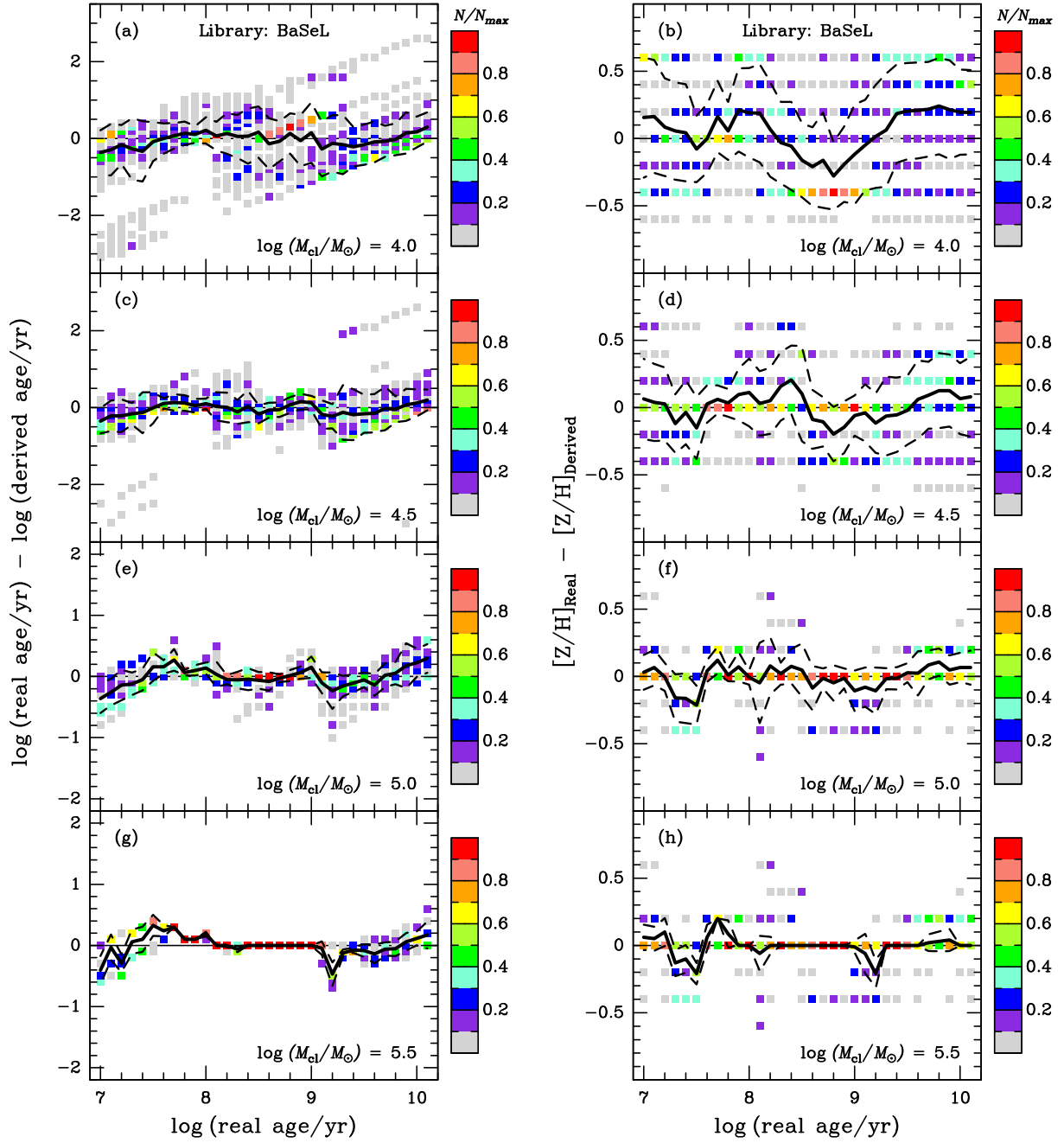


Figure A3. Similar to Figure A1, but now for the red optical range.

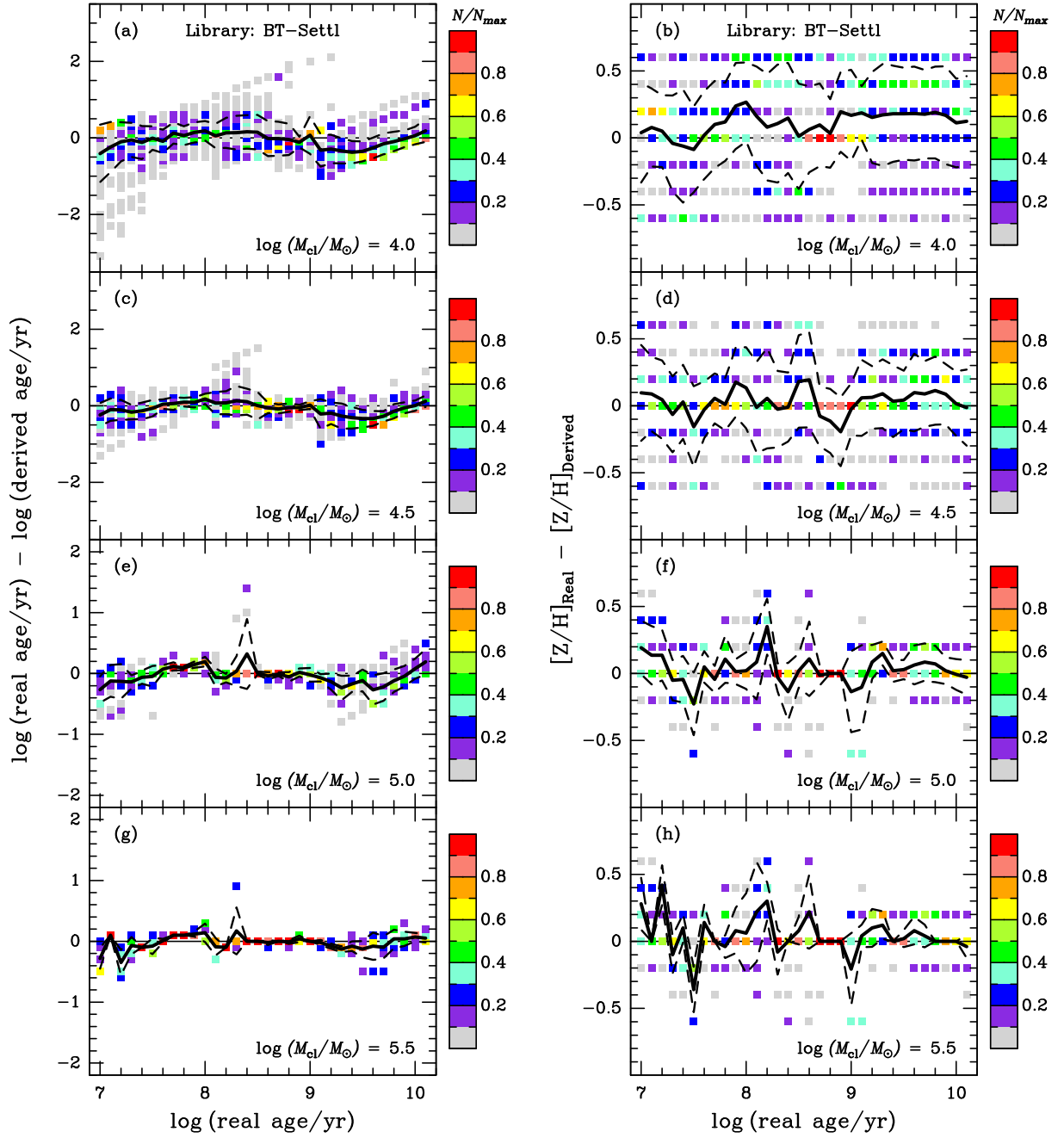


Figure A4. Similar to Figure A2, but now for the red optical range.

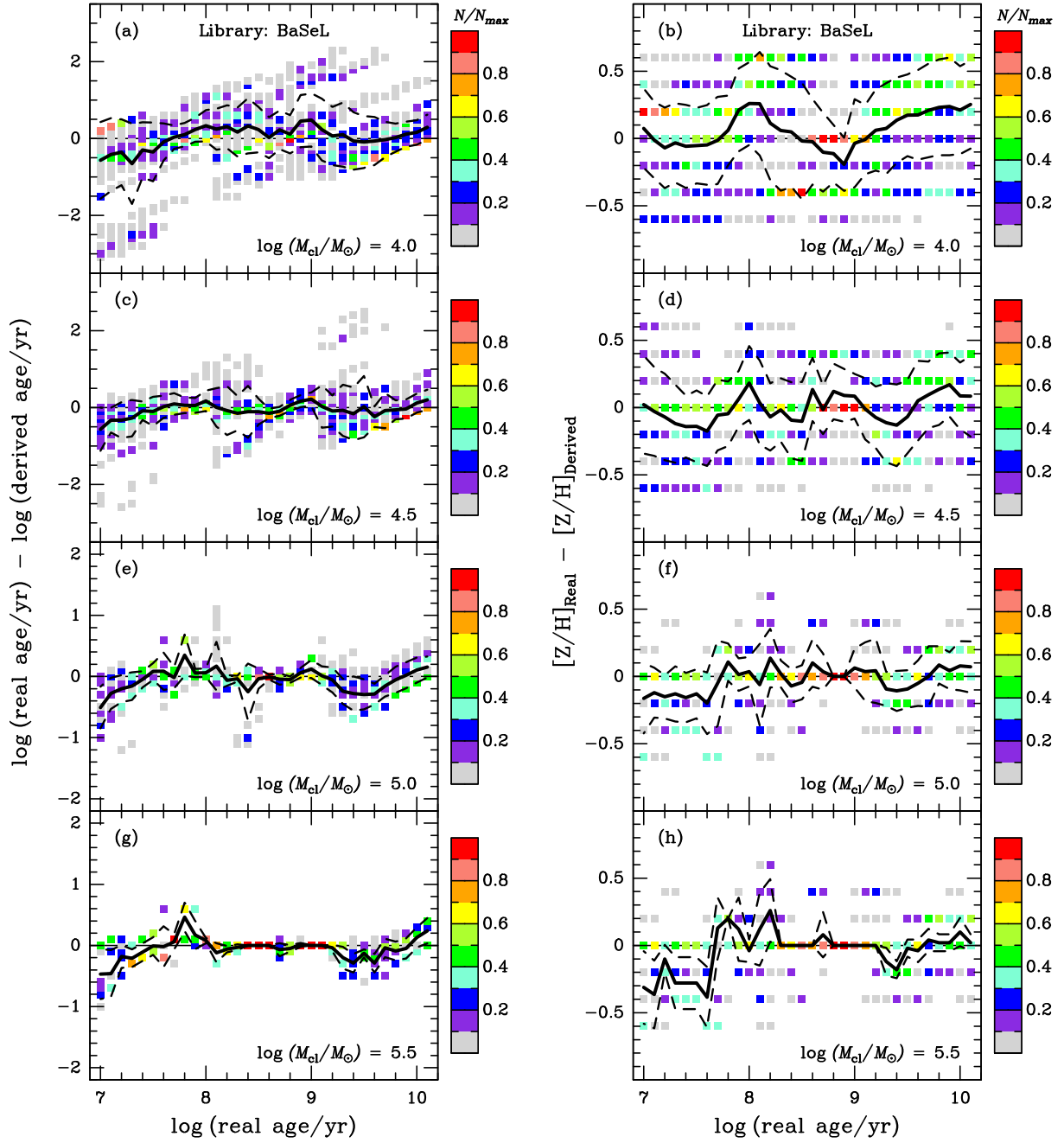


Figure A5. Similar to Figure A1, but now for the NIR range.

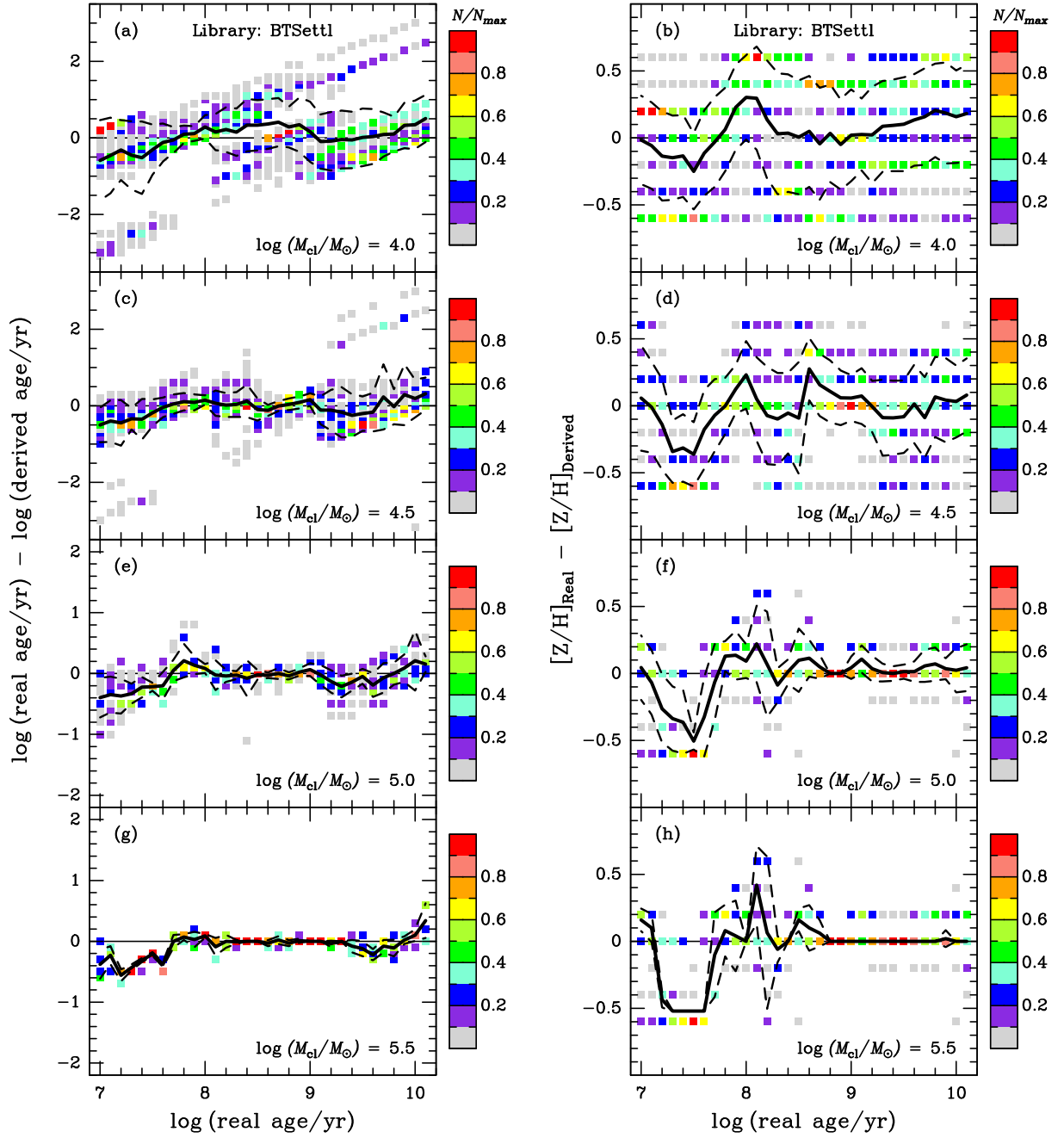


Figure A6. Similar to Figure A2, but now for the NIR range.

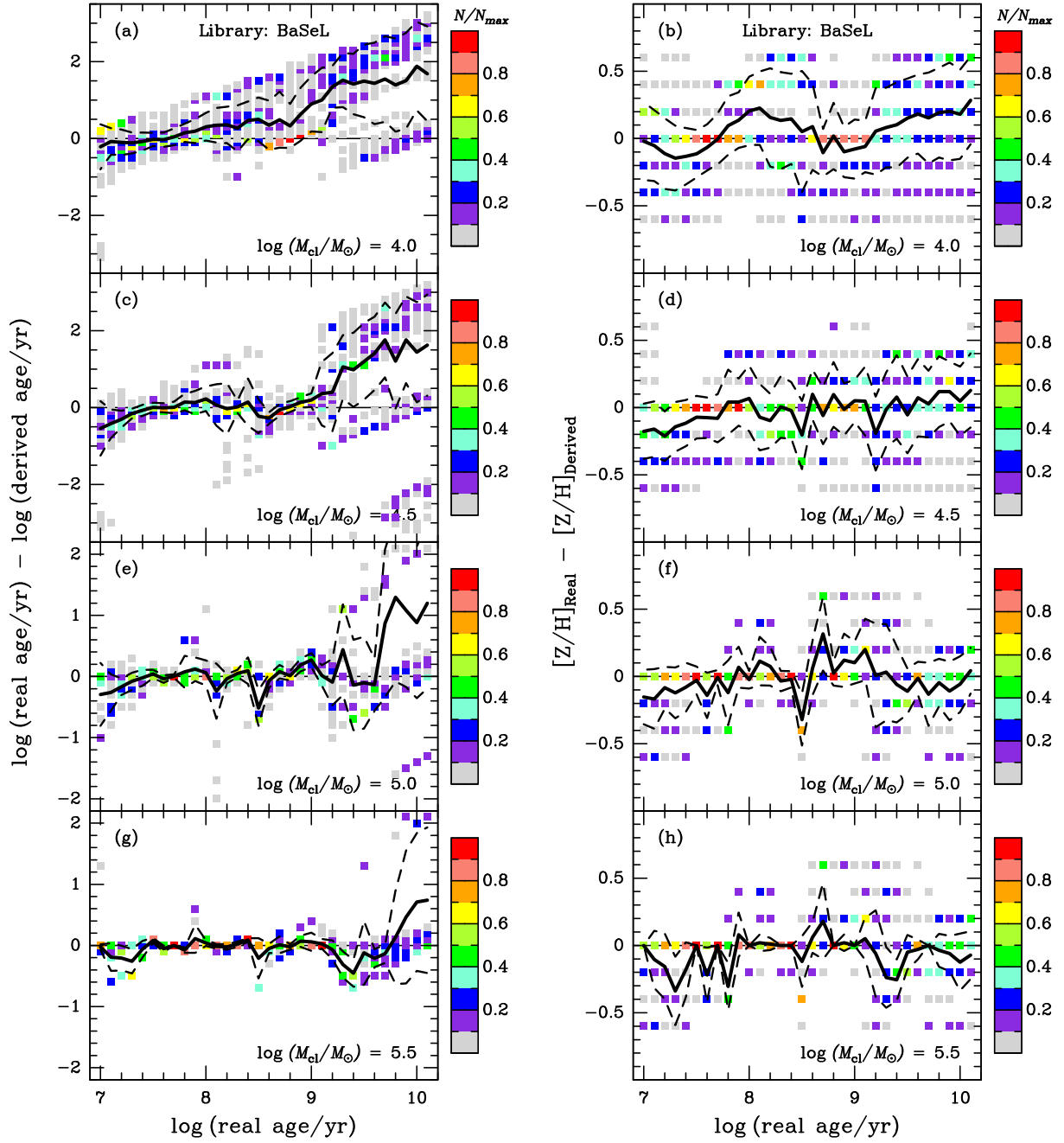


Figure A7. Similar to Figure A1, but now for the mid-IR range.

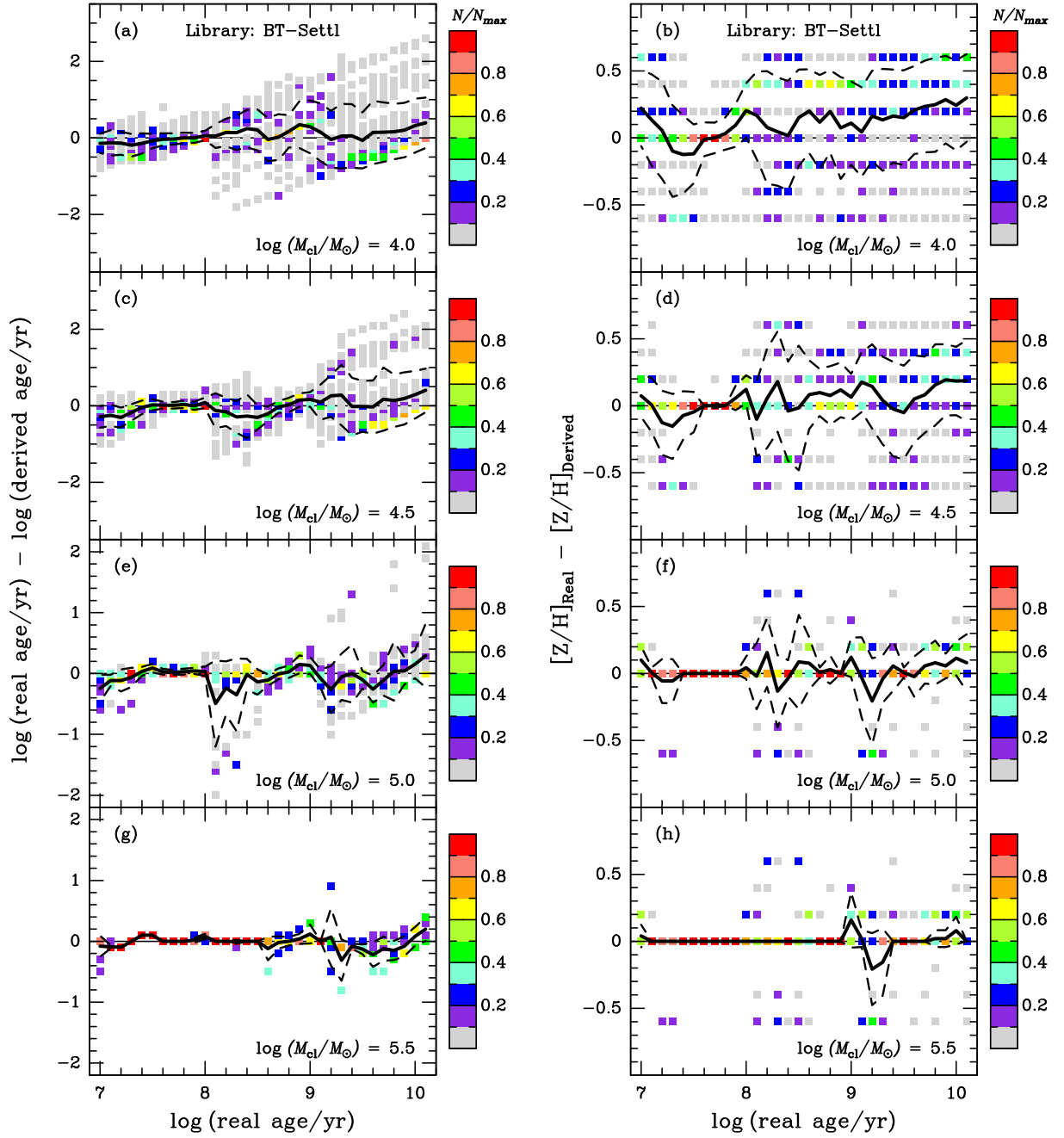


Figure A8. Similar to Figure A2, but now for the mid-IR range.